# *Colloquium*: Coherent diffusion of polaritons in atomic media

O. Firstenberg

*Department of Physics, Technion-Israel Institute of Technology, Haifa 32000, Israel and Department of Physics, Harvard University, Cambridge, Massachusetts 02138, USA*

M. Shuker

*Department of Physics, Technion-Israel Institute of Technology, Haifa 32000, Israel*

A. Ron

*Department of Physics, Technion-Israel Institute of Technology, Haifa 32000, Israel*

N. Davidson

*Department of Physics of Complex Systems, Weizmann Institute of Science, Rehovot 76100, Israel*

(published 8 July 2013)

Coherent diffusion pertains to the motion of atomic dipoles experiencing frequent collisions in vapor while maintaining their coherence. Recent theoretical and experimental studies on the effect of coherent diffusion on key Raman processes, namely, Raman spectroscopy, slow polariton propagation, and stored light, are reviewed in this Colloquium.

DOI: 10.1103/RevModPhys.85.941 PACS numbers: 42.50.Gy, 32.70.Jz, 51.20.+d, 71.36.+c

**CONTENTS**



## I. INTRODUCTION

Coherent Raman processes, in which two or more electromagnetic modes resonantly dress and excite an atomiclike system, provide a powerful interface between light and matter. They are potentially a cornerstone for future quantum information schemes and quantum-technology sensors, allowing the initialization, control, and monitoring of the quantum state of either the material or the light. Various Raman processes have been studied to date, namely, coherent population trapping (CPT) (Arimondo, 1996a), nonlinear magneto-optical rotation (NMOR) (Budker *et al.*, 2002), electromagnetically induced transparency (EIT) (Fleischhauer, Imamoglu, and Marangos, 2005), and slow and stored light (Lukin, 2003; Hammerer, Sørensen, and Polzik, 2010). These were all first demonstrated in a hot atomic vapor, perhaps the epitome of quantum-optics systems, combining high optical depth, low relaxation rates, and weak atom-atom interactions with the simplicity of both the experiments and the theoretical modeling. Indeed from the pioneering work of Alzetta *et al.* (1976) and Arimondo and Orriols (1976) on dark resonances, through later manifestations of elaborate Raman processes and dark-state polaritons (Harris, 1997; Budker *et al.*, 1999; Phillips *et al.*, 2001), and to state-of-the-art magnetometers, gyrometers, and miniature atomic clocks (Knappe *et al.*, 2004; Budker and Romalis, 2007; Smiciklas *et al.*, 2011) thermal atomic media have been at the frontier of experimental progress.

Two profound mechanisms underlie the dynamics of coherent processes in vapor: the continuous thermal motion of the atoms and the collisions among themselves and with the walls of the vapor cell. Collisions damage the internal atomic quantum state and set an upper limit on the coherence time of the system. Although a record coherence time of 1 min was recently obtained by Balabas *et al.* (2010) with an antirelaxation coating of the inner glass walls, it is often desirable to add a foreign buffer gas into the cell to delay the active atoms from leaving the illuminated region and approaching the walls (Happer, 1972). Selected species, such as noble gases or nitrogen molecules, have been known for many years to preserve the ground-state coherence of alkali-metal atoms upon collisions (Walker, 1989). Buffered cells are now commonly used in coherent Raman experiments (Ezekiel *et al.*, 1995; Graf *et al.*, 1995; Brandt *et al.*, 1997).

 

Nevertheless, even if one assumes perfect coherent-preserving collisions, the rapid fluctuations in the velocity of the active atoms modify their interaction with light. Dicke (1953) was the first to model a moving radiator undergoing frequent velocity changes. Dicke predicted that, when collisions dominate, the Doppler-broadened spectrum of a thermal gas will be narrowed, an effect known as *Dicke narrowing*. Dicke narrowing is closely related to motional narrowing in NMR, treated previously in the pioneering paper by Bloembergen, Purcell, and Pound (1948). Subsequently, Galatry (1961) formulated the spectral line shape of a thermal atom undergoing frequent collisions in a buffer gas. Nevertheless it was only in 2003 when a signature of Dicke narrowing was detected in the optical regime (Dutier *et al.*, 2003), because of the fundamental requirements that (a) the atomic coherence associated with the excited dipole be preserved during a collision, and (b) the mean free path between collisions $\Lambda$ be much smaller than the wavelength $\lambda = 2\pi/|\mathbf{q}|$ ($\mathbf{q}$ is the wave vector).

In contrast to optical transitions, both requirements are easily satisfied for Raman processes within a single electronic level. A collision with a typical buffer gas depends very weakly on the hyperfine or Zeeman substates and preserves their mutual coherence. At the same time, the relevant wave vector for the Doppler and Dicke mechanisms is due to the difference between the two Raman fields $\mathbf{k} = \mathbf{q} - \mathbf{q}_c$, leading to the *residual* Doppler and Dicke effects (Cyr, Tetu, and Breton, 1993). Broadening is totally avoided in the so-called Doppler-free arrangement $\mathbf{k} = \mathbf{q} - \mathbf{q} = 0$, in which one light beam excites an atom and a collinear beam of the same frequency deexcites it. However, in general either a small angular deviation or a small frequency difference between the two beams yields a nonzero Raman wavelength $\lambda_R = 2\pi/|\mathbf{k}|$ as small as a micrometer or as large as a centimeter, which affects the process. Residual Dicke narrowing of a Raman transition at the GHz frequency range is therefore readily obtained at moderate buffer-gas pressures, as exemplified in Fig. 1 for a Raman dark resonance. Correspondingly, general multimode light fields that span a spectrum in $\mathbf{k}$ space exhibit a generalized motional effect.

From the spatial viewpoint, the consequence of velocity-changing collisions in buffered cells is a Brownian or diffusion motion of the atoms. The internal atomic dipoles, e.g., those corresponding to the superposition between the two Raman levels, diffuse across the variations of the light fields. It is the near degeneracy of the Raman levels and the relatively large Raman wavelength that make the coherent diffusion effectual. The spatial effect is most clearly appreciated in light-storage experiments, in which the relative amplitude of the Raman fields is imprinted onto the spatial field of dipoles, which subsequently undergoes diffusion. The evolution becomes more complicated in slow-light experiments, in which the propagation of polaritons (a combined excitation of light and atomic coherence) is affected simultaneously by optical diffraction and atomic diffusion.

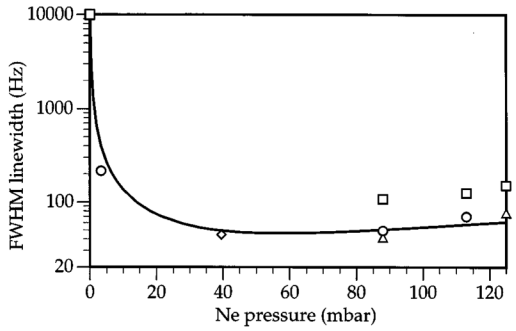


FIG. 1. Measured and calculated linewidths of a hyperfine dark resonance in rubidium, demonstrating the reduction in both the Doppler and transit-time broadenings with increasing pressure of neon buffer gas. Laser intensities are (squares) 17, (triangles) 11, (circles) 6, and (diamond) 1 mW/cm$^2$. From Brandt *et al.*, 1997.

This field of research is largely motivated by applications, namely, high-precision measurements, especially with spatial multipixel resolution (Kominis *et al.*, 2003), multimode quantum memories (Vasilyev, Sokolov, and Polzik, 2010), and spatial information processing, either classical or quantum (Marino *et al.* (2009). Atomic motion crucially affects the spectral and spatial resolution, sensitivity, and coherence time of these applications.

In this Colloquium, we review the recent progress in the understanding of motional effects in Raman processes. Spin exchange among the active atoms and with a polarizable buffer gas (Walker and Happer, 1997) as well as pressure broadening (Peach, 1981; Corey and McCourt, 1984) is beyond the scope of this paper. We mostly emphasize the regime of a dense inert buffer gas, in which the active atoms undergo perfect diffusion in the medium, and employ the complementary spectroscopic and spatial viewpoints. In doing so, we hope to illustrate the underlying mechanisms and their consequences in hot atomic media as well as in similar systems.

## II. RAMAN SPECTRA OF DIFFUSING ATOMS

### A. The Doppler-Dicke transition

The Doppler shift of an emitter moving at a velocity $\mathbf{v}$ is given by $\omega_{\text{Doppler}} = \mathbf{v} \cdot \mathbf{q}$. The spectrum exhibits sidebands at $\pm\mathbf{v} \cdot \mathbf{q}$, if the emitter is confined within two walls and periodically flips its direction. Dicke (1953) showed that, when the collisions are frequent, spectral components at the original frequency as well as higher-order harmonics emerge. For very frequent collisions, the carrier prevails, completely suppressing the Doppler effect. The distance between collisions $\Lambda$, with respect to the radiation wavelength $\lambda$, determines the narrowing factor. A movie in the Supplementary Material (161) illustrates the Doppler-Dicke transition for a moving acoustic emitter, obtained numerically by following Dicke (1953).

Doppler broadening in vapor originates from a picture of individual atoms distributed among velocity groups and experiencing distinct Doppler shifts. The Maxwell-Boltzmann distribution $F(\mathbf{v}) = (2\pi v_T^2)^{-3/2} e^{-v^2/(2v_T^2)}$ results in an inhomogenous spectral broadening of

$$\Gamma_{\text{Doppler}} = v_T |\mathbf{q}|, \tag{1}$$

where $v_T = \sqrt{k_B T/m}$ is the thermal velocity and $m$ is the atomic mass ($\Gamma_{\text{Doppler}}$ refers to $1\sigma$).

In a buffer-gas environment or due to confined cell geometries, the velocity-groups picture breaks down, as collisions

redistribute the velocities faster than it takes the resonance to stabilize. Consequently, as we establish in this section, the light merely faces fluctuations in the atomic velocities, leading to a crossover from the Gaussian (inhomogenous) to a Lorentzian (homogenous) line shape. The average velocity associated with these fluctuations is reduced with respect to $v_T$ by the Dicke narrowing factor $2\pi\Lambda/\lambda$. The homogenous Dicke half-width is thus given by (Galatry, 1961)

$$\Gamma_{\text{Dicke}} \approx 2\pi\frac{\Lambda}{\lambda}\Gamma_{\text{Doppler}} \ll \Gamma_{\text{Doppler}}. \tag{2}$$

The Doppler effect corresponds to a ballistic motion of the atoms ($\Lambda \gg \lambda$) and the Dicke effect to a diffusive motion ($\Lambda \ll \lambda$). One finds that $\Gamma_{\text{Dicke}}$ is proportional to the diffusion coefficient $D = v_T\Lambda$ and quadratic in the radiation wave number (Nelkin and Ghatak, 1964; Corey and McCourt, 1984),

$$\Gamma_{\text{Dicke}} = D|\mathbf{q}|^2. \tag{3}$$

Equations (1) and (2) can intuitively be understood as the inverse time an atom travels a distance $\lambda$ ballistically ($\propto \lambda/v_T$) or diffusively ($\propto \lambda^2/D$). Therefore, they are also interpreted as a transit-time broadening as illustrated in Fig. 2. At low buffer-gas densities, when the mean-free path is comparable to the wavelength ($\lambda/\Lambda \sim 2\pi$), the spectral width can be expressed as (Rautian and Sobel'man, 1967)

$$\Gamma_{\text{Doppler-Dicke}} = \frac{v_T}{\Lambda}\frac{4}{a^2}H\left(2\pi a\frac{\Lambda}{\lambda}\right), \tag{4}$$

where $a^2 = 2/\ln 2$, and $H(x) = e^{-x} - 1 + x$ conveys at its limits the Doppler trend $[H(x \to \infty) = x]$ and the Dicke trend $[H(x \to 0) = x^2/2]$.

For Dicke narrowing to occur, it is required and implicitly assumed in the models that the collisions themselves have a negligible effect on the internal atomic state. Unfortunately, this is not the case for optical resonances, where the collision interaction is different for the ground and excited levels, leading to decoherence and phase shifts of the optical dipole (Berman, 1982). The resulting *pressure broadening* of the spectral line increases with the buffer-gas density and becomes larger than the Doppler width much before the condition $\Lambda \ll \lambda$ for Dicke narrowing is satisfied. For instance, room-temperature rubidium with $v_T \approx 170$ m/s exhibits $\Gamma_{\text{Doppler}} \approx 220$ MHz at $\lambda = 780$ nm. For this wavelength, neon buffer gas at a pressure of about 200 torr is required for entering the Dicke regime $2\pi\Lambda/\lambda \sim 1$, but then the pressure broadening is already 2 GHz (Ottinger *et al.*, 1975). Optical Dicke narrowing thus cannot be observed in nearly all thermal media.

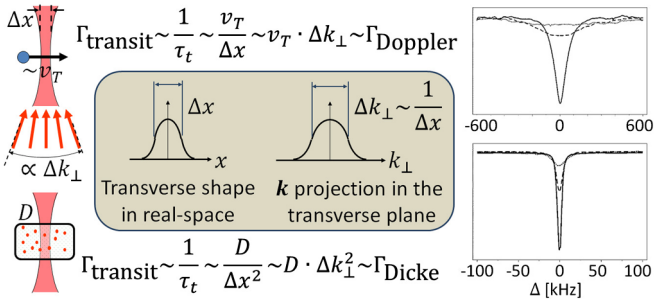


FIG. 2 (color online). Transit-time interpretation of the Doppler and Dicke effects. A beam of width $\Delta x$ has a span $\Delta k_\perp \sim 1/\Delta x$ of transverse momenta. The interaction time for an atom crossing the beam with velocity $v_T$ (top) is $\tau_t = \Delta x/v_T$, resulting in a transit-time broadening of $v_T\Delta k_\perp \sim \Gamma_{\text{Doppler}}$. For diffusing atoms (bottom), the mean interaction time is $\Delta x^2/D$, leading to a broadening of $D\Delta k_\perp^2 \sim \Gamma_{\text{Dicke}}$. Right: Dark resonances in rubidium vapor measured by Bolkart, Rostohar, and Weitz (2005) for a beam diameter $\Delta x = 5.6$ mm (top) without and (bottom) with 20 torr neon buffer gas. The respective linewidths are (solid lines) $2\Gamma_{\text{Doppler}} = 100$ kHz and $2\Gamma_{\text{Dicke}} = 6$ kHz. Dashed and dotted lines are measured with an angle between the Raman beams of $\theta = 0.31$ mrad and $\theta = 0.62$ mrad, respectively. Adapted from Bolkart, Rostohar, and Weitz, 2005.

In contrast, ground-state atomic transitions survive millions of collisions with the buffer gas before decohering. Since the associated microwave and rf wavelengths are much larger than the optical wavelength, Dicke narrowing becomes far more reachable (Frueholz and Volk, 1985). Indeed, buffer gases at the 1–100 torr levels have been used since 1955 to delay the atomic motion and reduce Doppler and transit-time broadening while maintaining long coherence times (Happer, 1972). As laid out by Cyr, Tetu, and Breton (1993) and discussed in what follows, two-photon transitions in the ground state, namely, the Raman and Rayleigh processes, exhibit roughly the same motional broadening behavior, with necessary adjustments mostly due to optical Doppler effects. We concentrate in the rest of this section on Dicke narrowing, which occurs already for plane waves, and discuss *Ramsey* narrowing in partially illuminated cells in Sec. V.

### B. Motional broadening in Raman processes

We consider as a model system dark resonances created via EIT in a $\Lambda$ configuration, depicted in Fig. 3(a). In $\Lambda$-EIT, a *probe* field $\mathbf{E}$ and a *coupling* field $\mathbf{E}_c$ couple two states from the atomic ground level ($|1\rangle$ and $|2\rangle$) to a common excited state ($|3\rangle$). The fields are hereafter taken to be classical and characterized by the Rabi frequencies $\Omega$ and $\Omega_c$ via $\mathbf{E} = \text{Re}(\hbar\varepsilon\Omega/\mu_{31})$ and $\mathbf{E}_c = \text{Re}(\hbar\varepsilon_c\Omega_c/\mu_{32})$, where $\varepsilon$, $\varepsilon_c$ are the field polarizations and $\mu_{31}$, $\mu_{32}$ are the transition dipole

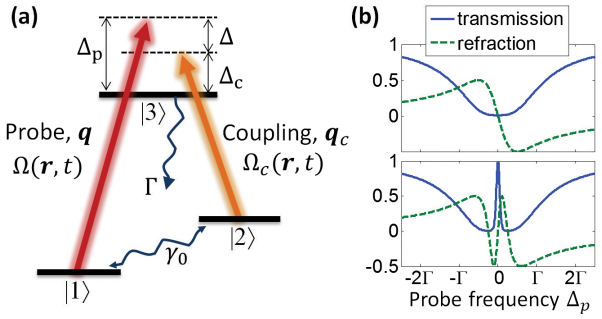


FIG. 3 (color online). Electromagnetically induced transparency in a $\Lambda$ scheme. (a) The Raman resonance $|1\rangle \leftrightarrow |2\rangle$ is excited via the state $|3\rangle$ by "probe" and "coupling" light fields. (b) Top: Transmission of the probe (solid line) in the absence of the coupling field and accompanied refraction (dashed line). Bottom: Dark resonance induced by the coupling field.

moments. In the absence of the coupling field, the probe experiences resonant absorption $\exp(-2\alpha L)$, determined by the absorption coefficient $2\alpha$ and the medium length $L$. The combined action of the probe and the coupling fields (the latter being usually much stronger, $|\Omega_c|^2 \gg |\Omega|^2$) drives the atoms into a dark state—a coherent superposition of the two lower states that inhibits the absorption of the probe, rendering the medium transparent. One can easily verify that the dark state on resonance $\Omega_c^*|1\rangle - \Omega^*|2\rangle$ is decoupled from the excited state $|3\rangle$ under the influence of the interaction Hamiltonian

$$H_I = -\hbar\Omega|3\rangle\langle 1| - \hbar\Omega_c|3\rangle\langle 2| + \text{H.c.}, \tag{5}$$

essentially due to destructive interference between the two excitation paths to $|3\rangle$.

The dark resonance depends on the two-photon (Raman) detuning $\Delta = \Delta_p - \Delta_c$ where $\Delta_p$ and $\Delta_c$ are, respectively, the one-photon (optical) detunings of the probe and coupling fields, and requires that $\Delta$ be smaller than the Raman linewidth. The latter varies from Hz to tens of MHz in thermal vapor and is determined primarily by the ground-state decoherence rate $\gamma_0$, power broadening from the coupling light, and motional broadening. For comparison, in most cases, the optical linewidth $\Gamma$ is much larger, varying from a few MHz for stationary (cold) atoms to a few hundreds of MHz in Doppler-broadened systems. Therefore a narrow transparency window forms at $\Delta_p = \Delta_c$ within the optical absorption line (Boller, Imamolu, and Harris, 1991), as can be seen in Fig. 3(b). At the same time, the probe also experiences very steep dispersion $\omega(dn/d\omega) \gg 1$ (dashed curve), leading to a much reduced group velocity. Ultranarrow dark resonances are used in a wide variety of processes, such as slow light (Hau *et al.*, 1999), stored light (Lukin, 2003), and nonlinear optics at low light levels (Harris and Hau, 1999; Peyronel *et al.*, 2012).

The Raman detuning is sensitive to the difference between the Doppler shifts of the probe and the coupling fields. When $\mathbf{q} = \mathbf{q}_c$, there is no residual Doppler effect, and only the optical transitions are Doppler broadened. In a general situation, however, the Raman wave vector

$$\mathbf{k} = \mathbf{q} - \mathbf{q}_c \tag{6}$$

does not vanish, and the expected residual widths are

$$\Gamma^{\text{res}}_{\text{Doppler}} = v_T k, \qquad \Gamma^{\text{res}}_{\text{Dicke}} = Dk^2, \tag{7}$$

where $k = |\mathbf{k}|$. The ratio between $\Gamma^{\text{res}}_{\text{Dicke}}$ and $\Gamma^{\text{res}}_{\text{Doppler}}$, the Dicke narrowing factor, ranges between $10^{-1}$ and $10^{-5}$ for typical experimental conditions.

A chief example is the dark resonance among the two hyperfine sublevels of ground-state alkali atoms, such as rubidium or cesium (Akulshin, Celikov, and Velichansky, 1991). The hyperfine splitting, on the order of a few GHz, results in a Raman wavelength $\lambda_R = 2\pi/k$ on the order of a few centimeters for collinear beams, implying a residual Doppler width of tens of kHz in the absence of a buffer gas. With a typical buffer-gas pressure of 10 torr, the mean-free path of the alkali atoms in the buffer gas is on the order of micrometers (alkali-alkali collisions cause decoherence but are much more rare). The narrowing factor is therefore on the order of $\Lambda/\lambda_R = 10^{-4}$, eliminating completely the residual Doppler effect. A systematic measurement of Dicke narrowing in dark resonances was reported by Brandt *et al.* (1997) for cesium (see Fig. 1), and later on by Erhard, Nußmann, and Helm (2000) for rubidium, accompanied by a numerical model (Erhard and Helm, 2001). The remaining homogenous width, due to alkali-alkali collisions, transit-time broadening, wall collisions, and spin-destruction collisions with the buffer gas, is on the order of tens of Hz, enabling the implementation of high accuracy all-optical frequency standards (Cyr, Tetu, and Breton, 1993; Nagel *et al.*, 1999; Knappe *et al.*, 2004).

Carvalho, de Araujo, and Tabosa (2004) measured the residual Doppler broadening in hyperfine dark resonances by introducing an angular deviation $\theta$ between the probe and the coupling beams. Measurements of residual Dicke narrowing in buffered cells were performed by Bolkart, Rostohar, and Weitz (2005) (see Fig. 2, right) and Shuker *et al.* (2007) (see Fig. 4) in a degenerate $\Lambda$ scheme, using two Zeeman states from the same hyperfine level so that $|\mathbf{q}| = |\mathbf{q}_c|$. In this scheme, $k = |\mathbf{q} - \mathbf{q}_c| \approx \theta|\mathbf{q}|$ for small $\theta$, featuring $\lambda_R \approx 1$ mm for $\theta = 1$ mrad. For a mean free path of a few micrometers, one finds $\lambda < \Lambda \ll \lambda_R$, i.e., the Raman resonance is in the Dicke regime, while the optical resonance ($\lambda \lesssim 1$ $\mu$m) is Doppler broadened. The latter is virtually insensitive to $\theta$ and can be as large as a few GHz, also due to pressure broadening. The $\theta$ dependence in Fig. 4 exhibits the quadratic signature of diffusion, with a clear narrowing effect: at $\theta = 0.5$ mrad, the measured width is $\Gamma^{\text{res}}_{\text{Dicke}} = 2$ kHz, much smaller than $\Gamma^{\text{res}}_{\text{Doppler}} = 250$ kHz. Note that the above studies were all done on one-photon resonance (EIT), while the Doppler-Dicke effect due to an angular deviation also manifests in off-resonance Raman transitions (Hosseini *et al.*, 2012), and in fact could be measured using off-resonant Rayleigh scattering with no incoming probe light (Berman, 2008).

The light intensity has a strong effect on the Raman spectra, due to optical pumping and the accompanying decoherence. The latter results in the so-called power broadening of the natural width $\gamma_0$. For an atom at rest, the optical-pumping rate and the EIT power broadening are given by

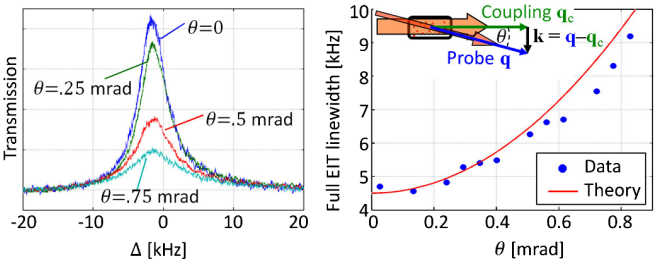


FIG. 4 (color online). Residual Doppler-Dicke broadening in EIT due to an angular deviation $\theta$ between the coupling and probe beams, measured in Rb vapor with 10 torr neon. The linewidth depends quadratically on $\theta$ as both the Doppler width ($\Gamma^{\text{res}}_{\text{Doppler}} = \theta\Gamma_{\text{Doppler}}$) and the Dicke narrowing factor ($2\pi\Lambda/\lambda_R = \theta\Lambda q$) are linear in $\theta$. The mean free path $\Lambda \approx 2$ $\mu$m used in the theory (right, solid line) corresponds to a collision rate of $\sim 10^8$/s and is calculated from the Rb-Ne collisional cross section (Gibble and Gallagher, 1991; Graf *et al.*, 1995). The broadening also leads to a decrease of the resonance transmission. Adapted from Shuker *et al.*, 2007.

$\gamma_p = |\Omega_c|^2/\Gamma$. Both become smaller in a Doppler-broadened medium, because the effectiveness of the pumping varies between the different velocity groups. This is a one-photon motional effect, in which each velocity group experiences different pumping and decoherence rates, providing inhomogenous "conditions" for the Raman process. The velocity-selective optical pumping (Aminoff and Pinard, 1982; Gawlik, 1986) results in correlations between the Raman and optical processes, similar to those employed in the well-known techniques of Doppler-free saturated-absorption spectroscopy (Hänsch, Shahin, and Schawlow, 1971) or laser-induced line narrowing (Feld and Javan, 1969). Naturally, buffer gas and velocity-changing collisions play an important role here, for example, by allowing the cumulative optical pumping of the whole Doppler profile or, alternatively, by limiting the interaction time with a certain velocity group (Bjorkholm, Liao, and Wokaun, 1982). These correlations were studied for dark resonances[1] in experiments by Ye and Zibrov (2002) and later by Figueroa *et al.* (2006) and Goldfarb *et al.* (2008), along with theoretical analysis by Javan *et al.* (2002) and Lee *et al.* (2003). Being essentially a one-photon effect, it is beyond the scope of this review; further details can be found in Ghosh *et al.* (2009) and Xiao (2009), and in references therein.

In the absence of additional relaxation, the spectral line at the extreme Doppler and Dicke limits is always, respectively, a Gaussian and a Lorentzian. In the intermediate regime, however, it is determined by the nature of the collisions. Depending mostly on the colliding species, the collisions may either be strong (= hard) or weak (= soft), resulting in, respectively, a large or small relative change in the velocity upon a single collision. A phenomenological characterization of the collision strength is given by Keilson and Storer (1952) in their popular collision kernel. For a given collision rate, the kernel renders the mean free path $\Lambda$ and the velocity correlation time $\gamma_c^{-1} = \Lambda/v_T$. There is a vast literature dealing with the sensitivity of atomic spectra to the nature of collisions; see Berman (1982), Rothberg and Bloembergen (1984), and Ciuryło *et al.* (2001), and references therein. Steady-state experiments, and spectroscopy, in particular, depend relatively weakly on the collision strength, as shown in Fig. 5. More elaborate schemes are required to directly quantify the collision kernels, e.g., coherent transient experiments such as the photon echo (Berman, 1982), or selective optical pumping of specific velocity groups and the subsequent probing of the velocity redistribution (Gibble and Gallagher, 1991; Morgan and Happer, 2010; McGuyer *et al.*, 2012). An analogous problem with trapped cold atoms undergoing elastic collisions was addressed by Sagi *et al.* (2010).

In this Colloquium we deal mostly with the limits $\lambda_R/\Lambda \gg 2\pi$ or $\lambda_R/\Lambda \ll 2\pi$, in which the collision strength has negligible effect. Detailed derivation of the spectra in the two regimes, i.e., the Gaussian process at the weak-collision limit or the Boltzmann relaxation at the strong-collision limit, and their equivalence in the far Doppler and Dicke limits are described in the Appendix.

[1]Even more intricate correlations arise in Raman schemes involving two coupling fields, such as four-wave mixing and electromagnetically induced absorption. Here the optical dipoles, and not only the ground state's populations and damping, become velocity dependent (Tilchin, Wilson-Gordon, and Firstenberg, 2011).

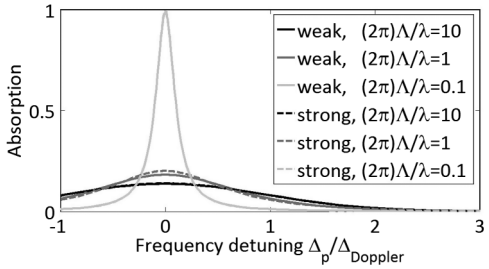


FIG. 5. Absorption spectra of thermal atoms. In the absence of collisions, the homogenous linewidth $\Gamma$ is dominated by the Doppler width $\Gamma_{\text{Doppler}} = 100\Gamma$. The transition from the (black) Doppler limit to the (light gray) Dicke limit occurs when the effective mean free path $\Lambda = v_T/\gamma_c$ ($\gamma_c^{-1}$ is the velocity correlation time due to collisions) is comparable to the wavelength $\lambda$ (dark gray). The spectra for the (solid line) weak and (dashed line) strong collisions are calculated from Eqs. (A4) and (A13), respectively. The differences between weak and strong collisions are not distinguishable at the far limits (black and light gray).

### C. The Raman resonance at the diffusion limit

Before concluding this section, we lay down the dynamic equations for the internal atomic state at the Dicke limit, when diffusion governs the Raman process. To elucidate the dynamics, we assume a weak probe field, to which the atomic response is linear. In fact, it is then sufficient to consider only two of the atomic dipoles, $\rho_{21}(\mathbf{r}, t)$ and $\rho_{31}(\mathbf{r}, t)$, associated with the ground-state and optical coherences, respectively. These are complex, slowly varying, spatial densities (envelopes of the oscillating dipoles), proportional to the atomic density $n_0$.

In the absence of a coupling field, a probe field with a slowly varying envelope $\Omega(\mathbf{r}, t)$ induces the optical dipole $\rho_{31}(\mathbf{r}, t) = in_0\Omega(\mathbf{r}, t)/\Gamma'$. The optical line shape is described by $1/\Gamma' = 1/\Gamma'(\Delta_p)$: a Lorentzian for stationary atoms ($\Gamma' = \Gamma + i\Delta_p$) and commonly a Voigt profile for a thermal gas (a convolution of the atomic Lorentzian line with the Gaussian Doppler distribution). In the case of frequent collisions, the optical line shapes given in Eq. (A4) or Eq. (A13) are to be used.

For a Raman process in the Dicke limit, Firstenberg *et al.* (2008) derived from Eqs. (A11) a set of equations for $\rho_{31}$ and $\rho_{21}$ near the Raman resonance ($\Delta_p \approx \Delta_c$), assuming nearly collinear fields $k = |\mathbf{q} - \mathbf{q}_c| \ll |\mathbf{q}|$:

$$\rho_{31}(\mathbf{r}, t) = \frac{i}{\Gamma'}[\Omega(\mathbf{r}, t)n_0 + \Omega_c(\mathbf{r})\rho_{21}(\mathbf{r}, t)], \tag{8}$$

where $\Omega_c(\mathbf{r})$ is the time-independent coupling field, and

$$[\partial_t - i\Delta + \gamma_0 + \gamma_P(\mathbf{r}) - D(\nabla + i\mathbf{k})^2]\rho_{21}(\mathbf{r}, t) = S(\mathbf{r}, t). \tag{9}$$

The ground-state dipoles $\rho_{21}(\mathbf{r}, t)$ obey a diffusionlike equation with the coefficient $D = v_T^2/\gamma_c$ ($\nabla$ is the gradient). The source term $S(\mathbf{r}, t) = -n_0\Omega_c^*(\mathbf{r})\Omega(\mathbf{r}, t)/\Gamma'$ is the two-photon

drive of the Raman transition, and $\gamma_P(\mathbf{r}) = |\Omega_c(\mathbf{r})|^2/\Gamma'$ is a spatially varying power-broadening rate. Notably, the atomic motion affects the transition both directly, by dephasing the Raman coherence, and indirectly via $\Gamma'$ and the power broadening.

It is important to realize that the diffusion term $D\nabla^2$ in Eq. (9) corresponds to the actual diffusion of the active atoms in the buffered cell. In fact, the description of spatial diffusion of the internal states of atoms and molecules in the form of Eq. (9) dates back to the seminal work by Torrey (1956) and has been the common practice for optical-pumping experiments in buffered cells (Happer, 1972; Bicchi *et al.*, 1980). Accordingly, the term $Dk^2$ (for nonstructured stationary beams $\partial_t = \nabla = 0$) accounts for the diffusion of atoms across the fields' interference pattern. The linear susceptibility[2] $\chi = (g/n_0)\rho_{31}/\Omega$, where $g = |\mathbf{q}|n_0|\mu_{31}|^2/\hbar\epsilon_0$ ($\epsilon_0$ is the vacuum permittivity), is then easily obtained from Eqs. (8) and (9),

$$\chi = \frac{ig}{\Gamma'}\left(1 - \frac{\gamma_P}{\gamma + Dk^2 - i\Delta}\right). \tag{10}$$

The two terms in the parentheses correspond to the optical and to the Raman resonances. On one-photon resonance, $\gamma \equiv \gamma_0 + \gamma_P$ is real and determines the EIT linewidth for stationary atoms, while the term $Dk^2$ expresses to the motional broadening (see Fig. 4).

## III. POLARITONS DYNAMICS IN DIFFUSIVE MEDIA

We have so far discussed the response of the atoms to a given arrangement of light beams from a spectroscopic viewpoint, but have not considered the spatial consequences of atomic motion. As these were taken into account in the description of the density-matrix dynamics, we can now directly apply the results of the previous section to the evolution of the structured light fields in space and time. The nonlocal response arising from the atomic motion and reflected in the dependence of the linear susceptibility on the wave vector has been demonstrated in recent years through various processes and, in particular, with slow light. In principle, it is the effective delay of the light, becoming comparable to the atomic motion through the beams, that renders these effects pronounced. That said, the description of the phenomena reviewed in this section is not always an obvious spatial consequence of atomic motion, and it is sometimes necessary to return to and employ the spectral picture of a manifold of Doppler-Dicke spectra.

Before doing so, it is instructive to consider a microscopic picture for the slow-light mechanism, going beyond the spectral interpretation of steep dispersion and transmission window. The propagation of resonant probe pulses in EIT is actually made possible by the continuous excitation and deexcitation of the Raman transition. Ahead of the pulse, the atoms are optically pumped into the "trivial" dark state $|1\rangle$; thereafter they stay in the dark state, while adiabatically following the probe pulse $\Omega(\mathbf{r}, t)$, going through $\Omega_c^*|1\rangle - \Omega(\mathbf{r}, t)^*|2\rangle$ and eventually returning to $|1\rangle$. The associated atomic coherence $\rho_{12}(\mathbf{r}, t)$ is always proportional to $\Omega(\mathbf{r}, t)$, and one is thus led to define a coupled excitation of light and matter in the form of a propagating polariton $\psi(\mathbf{r}, t) = \Omega(\mathbf{r}, t)\cos\eta - (\sqrt{gc}/n_0)\rho_{12}(\mathbf{r}, t)\sin\eta$ (Fleischhauer and Lukin, 2000). The mixing angle $\eta$ between the two components is controlled by the coupling field and determines the group velocity $v_g = c\cos^2\eta$. As expected, a lightlike polariton ($\eta \to 0$) travels at the speed of light, while a matterlike polariton ($\eta \to \pi/2$) stands still. Slower polaritons effectively "store" a larger fraction of the light as an atomic excitation, and hence their delayed propagation.

Polaritons structured in the plane normal to the propagation direction have been denoted as *slow images*, and they exhibit remarkable properties. A notable example is the delay and preservation of spatial quantum coherence and entanglement demonstrated by Marino *et al.* (2009). The "image" may be complex, having both amplitude and phase patterns, conforming to the amplitude and phase of the polariton's dark state. A typical setup for a slow-image experiment is shown in Fig. 6: while the coupling beam is large and uniform, the probe is patterned, imaged onto the cell, and eventually recorded. If the probe is also temporally modulated into a pulse, the pulse, and thus the whole image, is delayed in the medium.

The polariton velocity can be calculated from the linear susceptibility $v_g^{-1} = [d(\mathrm{Re}\chi)/d\Delta]_{\Delta=0}$ for $v_g \ll c$. At the diffusion limit, for nearly resonant light ($\Delta_c \approx \Delta_p \approx 0$, for which the damping rates $\Gamma'$ and $\gamma_P$ are real), Eq. (10) gives $v_g = (\gamma + Dk^2)^2/\alpha\gamma_P$. Here $2\alpha = 2g/\Gamma'$ is the absorption coefficient with no coupling field. As also shown by Kash *et al.* (1999) for the bufferless case (Doppler-broadened dark resonance), the group velocity is $k$ dependent and reverts to the known expression $v_g = \gamma^2/\alpha\gamma_P$ only for small enough $k$. For typical values in hot vapor $\gamma \approx \gamma_P \approx 10^1$–$10^6$ Hz and $\alpha \approx 1/\mathrm{cm}$, $v_g$ is on the order of m/s to km/s (Budker *et al.*, 1999). The group delay in a medium of length $L \approx$ 1–10 cm is then $\tau_d = L/v_g \approx$ 1–$10^5$ $\mu$s, easily comparable to the time at which atoms can travel through the beam, or through the 0.1–10 mm features of an image, in both buffered and

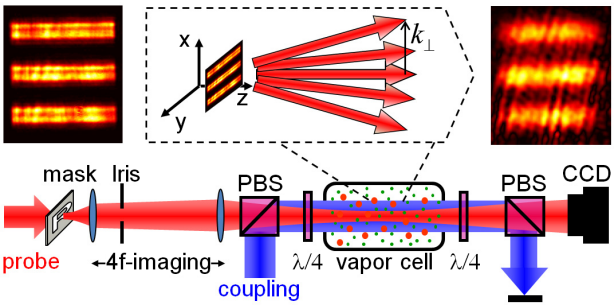


FIG. 6 (color online). Structured slow light. The probe beam is patterned by using a transmission mask, a grating, or a spatial light modulator and imaged onto the cell. An iris may be used to filter high frequencies and limit the angular span. After the cell, the probe is imaged onto a camera. Top: Diffusion of (left) a line pattern with 1.5 lines pair/mm after (right) 6 $\mu$m delay. [Measurements taken in a setup similar to that used by Shuker *et al.* (2008).]

[2]We define a linear susceptibility $\chi$, such that the transfer function of the probe field is $\exp(i\chi z)$, as opposed to the prevailing (unitless) definition $\exp(i|\mathbf{q}|\chi z/2)$ (Fleischhauer, Imamoglu, and Marangos, 2005).

bufferless cells. In contrast, slow images with 0.1-mm feature size delayed for only 10 ns using optical (not Raman) resonances by Camacho *et al.* (2007) showed no significant motional effects.

### A. Transverse spreading of light

The reflection of atomic motion in the spatial variation of slow light was preceded by extensive research on general spatial consequences of EIT and similar Raman processes. The emphasis, in the first experiments by Jain *et al.* (1995), Kasapi *et al.* (1995), and Moseley *et al.* (1995), and in the following years, was given to the implications of finite and inhomogenous strong beams, inducing inhomogenous absorption and refraction, and to the related effects of self-focusing and waveguiding. A direct observation of slow-light spreading due to atomic motion was reported by Pugatch *et al.* (2007), using a probe beam with a darkened (blocked) center. Images of the beam taken on and off resonance showed that the 50 $\mu$s slowing delay was enough for the atomic diffusion in the buffered cell to "fill" the 0.5-mm-diameter dark center almost completely. In effect, the ground-state dipoles diffusing to the center stimulate the conversion of coupling light into probe light. The phase pattern of the dipoles ensemble, originating from the incoming probe and coupling fields, acts as a directional source for this stimulated emission. In the alternative picture of polariton propagation, the filling of the center is interpreted as diffusion of the polaritons due to their atomic constituent.

A direct phase measurement of spreading light was reported by Xiao, Klein *et al.* (2008). Here the ballistic atomic motion in a bufferless, wall-coated cell is used to coherently transfer light between adjacent optical modes, as shown in Fig. 7. Atomic coherence is created at the input channel and maintained as the atoms spread in the cell. While longitudinal spreading has no significance in the degenerate arrangement used ($\mathbf{q} = \mathbf{q}_c$), the transverse spreading stimulates the coherent excitation of a propagating pulse in the second channel.

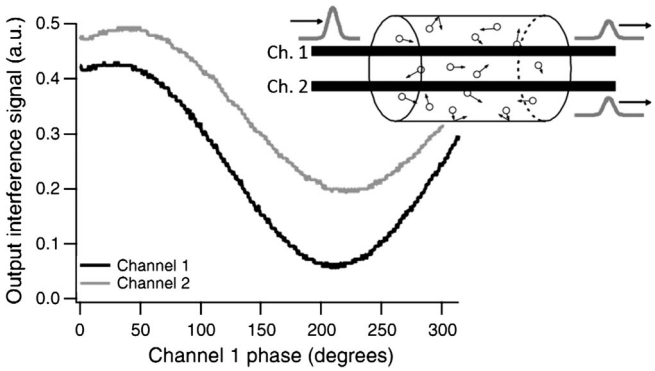


FIG. 7. Phase coherence between the two "output channels" of a slow-light beam splitter by Xiao, Klein *et al.* (2008). The atoms moving in the bufferless wall-coated cell mediate the coherence between the two channels. The measured transfer efficiency ($<5\%$) is a function of the slowing delay (0.5 ms), the decoherence due to wall collisions, and the beams and cell geometry. Optimization of these factors promises efficiencies close to unity. Adapted from Xiao, Klein *et al.*, 2008.

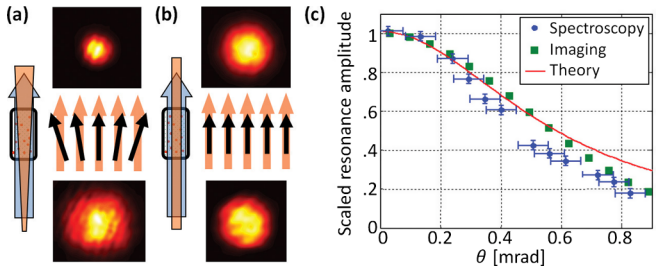


FIG. 8 (color online). Resonant transmission vs the angular deviation $\theta$ between the Raman beams. (a) Imaging experiment, measuring the resonant transmission of a diverging probe beam with a large (plane-wave) coupling beam. Pictures are taken beyond the cell by impinging the beams directly onto a CCD detector, (top) with and (bottom) without the atoms. Stronger absorption is observed away from the center, where, in the optical ray approximation, $\theta$ is larger. Maximal $\theta$ is $\sim$2 mrad at the beam radius. (b) A reference with a nondiverging probe. (c) Scaled transmission (squares) from the aforementioned imaging experiment and (circles) from spectroscopy (see Fig. 4). The theoretical curve is calculated from Eq. (11). Adapted from Shuker *et al.*, 2007.

To understand the spreading of light within the Doppler-Dicke context, we return to Eq. (10) with nearly resonant beams ($\Delta_p \approx \Delta_c \approx 0$), for which the absorption spectrum of the probe is given by

$$\mathrm{Im}\chi = \alpha\left[1 - \frac{\gamma_P(\gamma + Dk^2)}{(\gamma + Dk^2)^2 + \Delta^2}\right]. \tag{11}$$

The relative height at the center of the dark resonance ($\Delta = 0$) depends on the Raman wave number $k$ in the form of a Lorentzian $\gamma_P/(\gamma + Dk^2)$ of width $k_0 = (\gamma/D)^{1/2}$, as confirmed by Bolkart, Rostohar, and Weitz (2005) and Shuker *et al.* (2007) with a small deviation angle $\theta \approx k/|\mathbf{q}|$ between the coupling and probe beams (see Fig. 8). The dependency of the transmission on $\theta$ is manifested in experiments with nonuniform, structured, light fields, due to the angular span of beam. In the decomposition of the field into a manifold of superimposed plane waves, high-order transverse modes and finely patterned beams require a large angular span, which implies large Raman wave numbers (top sketch in Fig. 6). When these are attenuated due to motional broadening, the fine structure of the beam deteriorates. A maximum acceptance angle $\theta = k_0/|\mathbf{q}|$ thus sets a minimum "pixel" size of $2\pi/k_0$ that can be efficiently transmitted, whereas smaller features are bound to spread. So atomic motion, via motional broadening, results in the spreading of the light field.

### B. Diffusion and motional-induced diffraction

At certain conditions, motional broadening results in an exact diffusion of the slow polaritons as well as in a diffractionlike evolution. To this end, we employ the following arrangement: a plane-wave coupling field along the $z$ axis; a paraxial, nearly parallel, probe $\mathbf{q} \parallel \mathbf{q}_c$ with a finite envelope in the transverse plane $(x, y)$; and a nearly degenerate Raman scheme $|\mathbf{q}_c| \approx |\mathbf{q}| \equiv q$ so that the Raman wave vectors resulting from the probe's structure have a negligible $z$ component (hyperfine splitting with $\lambda_R$ on the order of centimeters is still permitted). Note that the choice $\mathbf{q} = \mathbf{q}_c$

still allows for a small angular deviation between the beams via a phase term $e^{i\theta qx}$ in the probe's envelope. In the paraxial approximation, the probe field obeys

$$\left(\frac{\partial_t}{c}+\partial_z-i\frac{\nabla_\perp^2}{2q}\right)\Omega(\mathbf{r},t)=i\frac{g}{n_0}\rho_{31}(\mathbf{r},t), \tag{12}$$

where $\nabla_\perp^2=\partial_x^2+\partial_y^2$ is the transverse Laplacian. Equations (8), (9), and (12) compose the full set of equations of motion for the slowly varying envelopes.

The group velocity $v_g$ obtained earlier in this section is applicable for pulses long enough such that their bandwidth (in the temporal frequency domain) is within the linear dispersion regime. If the pulses vary more slowly than any other rate in the system, the time dependence can be treated parametrically, based on a quasi-steady-state assumption. The steady-state assumption can easily be lifted within the linear response approximation, which is valid as long as the coupling field is stationary and uniform. Keeping in mind that the traveling pulses are essentially delayed, it will still be meaningful in quasi-steady state to translate distance to time via $v_g$.

The changes of the probe along $z$ are due to its finite extent (in a pulsed experiment) and due to absorption and refraction in the medium; both are assumed to vary much more slowly than the envelope in the transverse plane, making the diffusion negligible in the $z$ direction. The relevant Raman wave vectors are thus identical with the transverse spatial frequencies. Taking the Fourier transform $(x,y)\rightarrow(k_x,k_y)=\mathbf{k}_\perp$ of Eqs. (8), (9), and (12) while maintaining the explicit $z$ dependence, one recovers the linear susceptibility $\chi(\mathbf{k}_\perp)=i\alpha[1-\gamma_P/(\gamma+Dk_\perp^2-i\Delta)]$ and the steady-state evolution along $z$:

$$\partial_z\Omega(\mathbf{k}_\perp;z)=\left[i\chi(\mathbf{k}_\perp)-i\frac{k_\perp^2}{2q}\right]\Omega(\mathbf{k}_\perp;z). \tag{13}$$

Clearly the geometric effect of free-space diffraction $ik_\perp^2/(2q)$ influences slow images precisely as in free space. For a confined $k_\perp$ spectrum, the susceptibility can be expanded in orders of $k_\perp^2$ as $\chi(\mathbf{k}_\perp)=\chi_0+[\chi(\mathbf{k}_\perp)]_{\text{motional}}$, where $\chi_0=i\alpha[1-\gamma_P/(\gamma-i\Delta)]$ is the susceptibility for an atom at rest, and

$$iv_g[\chi(\mathbf{k}_\perp)]_{\text{motional}}=\frac{-\gamma^2}{(\gamma-i\Delta)^2}Dk_\perp^2+O(k_\perp^4), \tag{14}$$

with $v_g=\gamma^2/(\alpha\gamma_P)$. The $k_\perp^4$ term is negligible when the probe's spectrum is initially confined within $k_\perp\ll k_0=(\gamma/D)^{1/2}$. The requirement $k_\perp\ll k_0$ is usually stricter than the optical paraxial condition (for example, the typical values $D=10\ \text{cm}^2/\text{s}$ and $\gamma=10\ \text{kHz}$ give $k_0$ on the order of $0.01\ \mu\text{m}^{-1}$). Returning to $(x,y)$ space,

$$\partial_z\Omega=\left[i\chi_0+\left(\frac{\mathcal{D}}{v_g}+\frac{i}{2q}\right)\nabla_\perp^2+O(\nabla_\perp^4)\right]\Omega, \tag{15}$$

we find an effective complex diffusion coefficient:

$$\mathcal{D}=D\frac{1-(\Delta/\gamma)^2}{[1+(\Delta/\gamma)^2]^2}+iD\frac{2(\Delta/\gamma)}{[1+(\Delta/\gamma)^2]^2}. \tag{16}$$

The real part of $\mathcal{D}$ corresponds to an actual diffusion of the polariton. The imaginary part causes quadratic dispersion within the $k_\perp$ spectrum, with a functional form identical to that of the optical paraxial diffraction, and is thus referred to as motional-induced diffraction (MID).

On resonance $\Delta=0$, the polariton diffusion precisely matches the atomic diffusion $\mathcal{D}=D$. Besides an overall absorption and phase shift originating from $i\chi_0$, the evolution of the polariton is a linear sum of optical diffraction with respect to the distance traveled $(\partial_z\Omega)_{\text{diffraction}}=i\nabla_\perp^2\Omega/(2q)$ (due to the polaritons's light constituent) and atomic diffusion with respect to time $(\partial_t\Omega)_{\text{diffusion}}=D\nabla_\perp^2\Omega$ (due to its matter constituent). For the latter, we translated $v_g\partial_z\rightarrow\partial_t$. The relative weight of diffraction and diffusion is thus controlled by the group velocity. Off the Raman resonance $\Delta\neq0$, the polariton diffusion slows down. The real part of $\mathcal{D}$ decreases with increasing $|\Delta|$, until vanishing completely at $\Delta=\pm\gamma$. At this detuning, the polariton does not experience any standard diffusion, while the remaining $O(\nabla_\perp^4)$ term gives rise to subdiffusion evolution.

Moreover, at $\Delta\neq0$ the MID becomes nonzero and adds up to the optical diffraction. The detuning determines the sign of the MID, with $\text{Im}(\mathcal{D})>0$ at positive detuning adding to the optical diffraction, and $\text{Im}(\mathcal{D})<0$ at negative detuning negating it. While the maximum MID is obtained at $\Delta=\pm3^{-1/2}\gamma$, the more interesting case is $\Delta=\pm\gamma$, in which $\mathcal{D}=\pm iD/2$ is purely imaginary, inducing diffraction without diffusion. Here the ratio between $\pm D/v_g$ and $1/q$ determines the balance between the optical and induced diffraction, and, for given $D$ and $q$, it is governed by the group velocity.

Firstenberg, Shuker *et al.* (2009) proposed utilizing MID to completely eliminate the paraxial diffraction in the medium, by choosing $\Delta=-\gamma$ and $v_g=qD$. At these conditions, both the imaginary and real parts of the $\nabla_\perp^2$ coefficient vanish in Eq. (15), rendering a diffractionless, diffusionless medium. Conversely, at $\Delta=+\gamma$ the actual diffraction in the medium is twice that in free space. The nondiffraction condition $v_g=qD$ can intuitively be derived by requiring the diffusion spreading of a focused Gaussian beam to be equal to its diffraction spreading after one Rayleigh distance $z_R=qw_0^2/2$, where $w_0$ is the beam waist radius. Since the beam does not expand, it is virtually trapped in two dimensions by the diffusing atoms in an interesting analogy to the mechanism of Doppler cooling of atoms by red-detuned light. The latter also relates to a proposal by Kocharovskaya, Rostovtsev, and Scully (2001) to stop light propagation using one-photon detuning in a bufferless cell.

These effects were studied by Firstenberg, London *et al.* (2009) at the condition $v_g=qD$ and are demonstrated in Fig. 9: The image exhibits optical diffraction (far detuned), diffusion ($\Delta=0$), nondiffraction ($\Delta=-\gamma$), and double diffraction ($\Delta=+\gamma$). Shwa *et al.* (2012) examined the MID of an array of optical vortices as shown in Fig. 10.

An intuitive physical explanation to the suppression of *diffraction* is the "trapping" of the light by the moving atoms, in an analogous mechanism to the well-known Doppler trapping of atoms by light. Similar to Doppler trapping, due to the negative (red) detuning, an atom moving radially toward the optical axis couples better to the outgoing light components ($k_\perp>0$, see Fig. 6 top), effectively dragging them back to the axis. The suppression of *diffusion* is slightly more intricate as

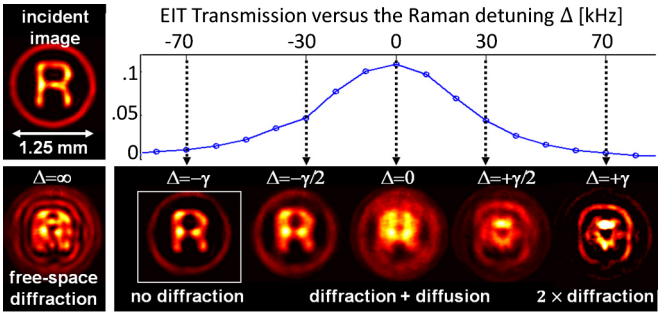


FIG. 9 (color online). Polariton diffusion and motional-induced diffraction. A Zeeman EIT setup is used, similar to that in Fig. 6, with a cell length $L = 5$ cm and optical depth $2\alpha L = 6$. The free-space diffraction (bottom left) is compared to transmitted slow images at several Raman detunings (right). At $\Delta = 0$, the polariton is delayed by $\sim 6$ $\mu$s and experiences the combination of optical diffraction and diffusion ($D = 11$ cm$^2$/s for 10 torr of neon). At $\Delta < 0$, both diffusion and diffraction are reduced, and at $\Delta = -\gamma \approx -70$ kHz, they are completely suppressed ($Dq = v_g \cong 8700$ m/s). Numerical calculations confirm that the small difference between the input image and the transmitted image at $\Delta = -\gamma$ is primarily due to residual $\nabla^4$ terms. At $\Delta = +\gamma$, no diffusion occurs, but the polariton experiences the sum of equal optical and motional-induced diffraction, as if the image has propagated a free-space distance of $2L$. Adapted from Firstenberg, London *et al.*, 2009.

it involves two competing processes as $k_\perp$ increases: faster dephasing of the Raman coherence, but smaller sensitivity to frequency detuning. As with any harmonic oscillator, there exists a specific driving frequency ($\Delta = \pm\gamma$) where the dissipated power does not depend on the dumping rate ($\gamma$) to first order, since the reduction in the amplitude of oscillations is compensated by the increase in friction. At this frequency, the transmission of the probe does not depend on $k_\perp$ and diffusion vanishes.

As mentioned, extensive study was devoted to the manipulation of diffraction by modulating the susceptibility in real space, with either the coupling beam, the probe beam, or the medium itself inducing the necessary inhomogeneity of the refraction index.[3] In all these schemes, specific transverse modes are maintained, but a general multimode field disperses and may perhaps regenerate after a certain self-imaging distance (Cheng and Han, 2007). In contrast, diffraction manipulation with linear optics in $k_\perp$ space, in the form of Eq. (15), applies to multimode fields with

[3]Electromagnetically induced focusing by an inhomogenous coupling field was realized by Moseley *et al.* (1995) in hot vapor and by Mitsunaga, Yamashita, and Inoue (2000) in a cold ensemble. Nondiffracting propagation of certain transverse modes due to nonuniformity of the coupling field was referred to as induced solitons (Bortman-Arbiv, Wilson-Gordon, and Friedmann, 1998), induced waveguides (Truscott *et al.*, 1999; Kapoor and Agarwal, 2000), and transverse confinement (Andre *et al.*, 2005; Cheng, Han, and Yan, 2005). Waveguiding was also demonstrated using the inhomogenous density in a cold atomic cloud (Vengalattore and Prentiss, 2005; Tarhan, Postacioglu, and Müstecaplioglu, 2007). Last, it was proposed that self-focusing via a Kerr-like effect will support spatial solitons (Hong, 2003; Friedler *et al.*, 2005).

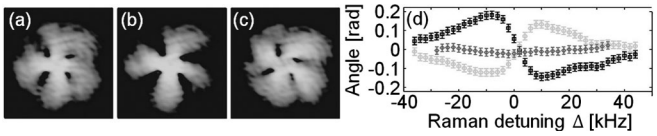


FIG. 10. Collective rotation of a vortex array due to induced diffraction by Shwa *et al.* (2012). Hyperfine EIT with $^{87}$Rb is performed in a cell of length $L = 7.5$ cm with 20 torr neon ($D = 6$ cm$^2$/s, $v_g = 5000$ m/s). An array of four $m = +1$ vortices (total angular momentum $J = 4$) rotates clockwise (b) at $\Delta = 0$, the same as it does in free space. (a) At $\Delta < 0$, the optical diffraction is counteracted, leading to a counterclockwise rotation with respect to $\Delta = 0$. (c) At $\Delta > 0$, diffraction is enhanced, leading to increased clockwise rotation. Images are $1 \times 1$ mm$^2$. (d) Rotation angle for a two-vortex array with (light gray circles) $J = 2$, (black squares) $J = -2$, and (dark gray diamonds) $J = 1 - 1 = 0$. All-optical control on the vortices motion could be useful for fast optical-trapping applications. Adapted from Shwa *et al.*, 2012.

arbitrary phase and intensity patterns. Since no actual waveguide is defined, the medium suspends the expansion of an incoming beam wherever it impinges on the input plane.

It is instructional to define an *index of diffraction* $n_{\rm diff} = (1 - qD/v_g)^{-1}$, equivalent to the index of refraction as far as paraxial diffraction is concerned. Without atomic motion ($D = 0$), diffraction is not altered ($n_{\rm diff} = 1$). At the nondiffraction conditions, the index diverges ($n_{\rm diff} \to \infty$). Snell's law $\sin\theta_i = n_{\rm diff} \sin\theta_r$ then implies no angular divergence inside the medium $\theta_r = 0$ regardless of the incident angle $\theta_i$ and hence no diffraction, as illustrated in Fig. 11(a).

Now consider the possibility of reducing $v_g$ below $qD$, still with $\Delta = -\gamma$, so that the (negative) MID be further strengthened. Then both the overall diffraction of the polariton and the index of diffraction become negative. The medium undoes a paraxial diffraction that already took place, manifesting a negative-index lens in the spirit of Vaselago (1968) and Pendry (2000). Remarkably, the imaging conditions of such a lens are insensitive to its position between the object and the image as shown for $n_{\rm diff} = -1$ in Fig. 12.

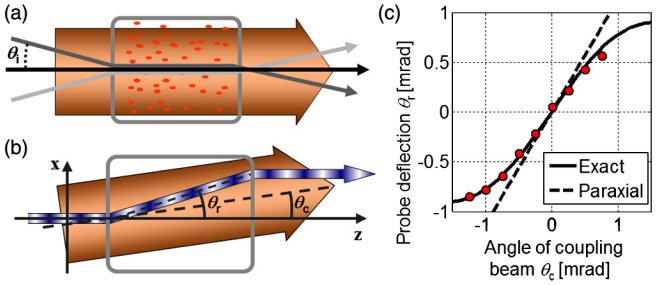


FIG. 11 (color online). Probe deflection. (a) Nondiffraction can be understood as the deflection of all rays into a common direction. The rays maintain their phase relations while traversing the medium and afterward deflect back into their original direction. (b) Generally, the probe beam deflects toward the direction of the coupling beam for $\Delta < 0$ and away from the coupling for $\Delta > 0$. At $\Delta = \pm\gamma$, a Snell-like law determines the ratio between $\theta_r$ and $\theta_c$. (c) In the nondiffraction conditions, the probe beam assumes the direction of the coupling beam for small enough angles (circles are measurement, lines are theory). Adapted from Firstenberg, London *et al.*, 2009.

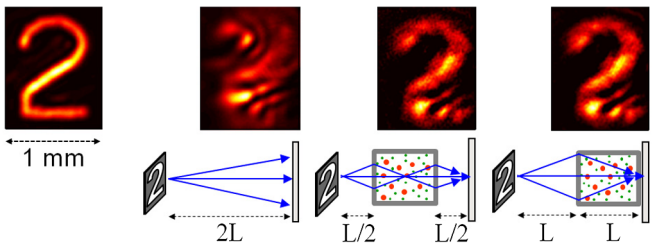


FIG. 12 (color online). Manifestation of a negative-diffraction lens with $n_{\rm diff} = -1$. The optical diffraction is exactly reversed by setting $v_g = Dq/2$, so that an image diffracting along a distance $L$ before the cell is reimaged at the end of the cell. The positive and negative diffractions "commute," e.g., it makes no difference if the positive diffraction occurs partly before and partly after the cell, as exemplified by the two right images. The restriction $k_\perp \ll k_0$ was not fulfilled in this experiment, hence the imperfections in the imaging. Solid arrows indicate geometrical rays (not $\mathbf{q}$ vectors) refracting oppositely to the incident angle $\theta_r = -\theta_i$, according to Snell's law $\sin\theta_i = n_{\rm diff}\sin\theta_r$, as expected in a negative-index material. Adapted from Firstenberg, London *et al.*, 2009.

An important caveat when working at large Raman detunings is the reduced transmission; even for high coupling intensities ($\gamma = \gamma_P$), the absorption at $\Delta = \pm\gamma$ cannot be rendered lower than $\mathrm{Im}\chi_0 \approx \alpha/2$. This translates to a low transmission, of about $\exp(-5)$, at the Rayleigh distance of a beam with $w_0 = \pi/k_0$, which is the minimal pixel size allowed under the $k_\perp \ll k_0$ condition. The experiments by Firstenberg, Shuker *et al.* (2009) took place under these conditions.

### C. Induced drift and artificial vector potential

The attentive reader may have already realized that, while $n_{\rm diff}$ alters the refraction at the entrance and the exit of the medium, it is the direction of the coupling beam that determines the virtual plane of incidence for this refraction. In fact, since the real index of refraction in dilute vapor is only marginally different than unity ($n = 1 \pm 10^{-6}$), the actual entrance plane of the cell has no optical significance. It is thus the virtual plane perpendicular to the coupling-beam direction which defines the incident and refraction angles for the modified Snell's law $\sin(\theta_i - \theta_c) = n_{\rm diff}\sin(\theta_r - \theta_c)$, where $\theta_c = 0$ for an axial coupling beam. Therefore, tilting the coupling beam results in an angular deflection of the probe beam in the cell. For a straight-on incidence ($\theta_i = 0$), the modified Snell's law yields $\theta_r = \theta_c(1 - n_{\rm diff}^{-1})$ [see Fig. 11(b)]. In particular, at the nondiffraction conditions ($n_{\rm diff} \to \infty$), the probe deflects exactly onto the direction of the coupling beam ($\theta_r = \theta_c$), as shown in Fig. 11(c).

Mathematically, tilting the coupling beam superimposes a transverse phase grating $\exp(ixq\theta_c)$ on the Raman interference pattern, replacing $Dk_\perp^2$ in Eq. (14) by $D(\mathbf{k}_\perp - q\theta_c\hat{\mathbf{x}})^2$. For angles small enough ($q\theta_c \ll k_0$), the resulting term in Eq. (15), $2(\mathcal{D}/v_g)\boldsymbol{\nabla}_\perp \cdot \hat{\mathbf{x}}q\theta_c$, induces a directional deflection on the probe at an angle $\theta_r = \mp(qD/v_g)\theta_c = \mp(1 - n_{\rm diff}^{-1})\theta_c$, in accordance with the modified Snell's law. It is worthwhile emphasizing that the deflection effect does not involve an actual refraction of the optical wave vector ($\mathbf{q}$). Similarly to the walk-off phenomenon in birefringent crystals, the wave fronts (equal phase planes) maintain their original orientation. Hence, the deflection is unobservable for plane waves and has meaning only for finite beams. In analogy to a group velocity, which can be modified either via $n$ or via the dispersion $dn/d\omega$, the deflection here is a (spatial) group effect, in which the transverse dispersion $\sim dn/dk_\perp$ changes the propagation trajectory.

In the popular analogy between paraxial light propagation and the Schrödinger dynamics of a massive particle in two dimensions, the wave vector plays the role of the mass. When the MID at $\Delta = \pm\gamma$ dominates the optical diffraction, and one translates $z \to v_g t$ in Eq. (15), the effective mass is $m = \pm\hbar/D$. A phase gradient imposed by the coupling fields thus translates to a vector potential (VP) for a charged particle:

$$i\hbar\partial_t\Omega(x,y) = \frac{1}{2m}(i\hbar\nabla_\perp + e\mathbf{A})^2\Omega(x,y), \tag{17}$$

where $\mathbf{A} = i\hbar\nabla_\perp \ln\Omega_c^*(\mathbf{r})$ and $e = 1$.

As reviewed by Dalibard *et al.* (2011), artificial VP created by the optical dressing of neutral atoms is a major field of study. Here, however, the polaritons, and not the atoms themselves, experience the artificial VP. As a result, the coupling beam can be used to mimic the operation of electromagnetic fields on the polariton. In particular, a tilted coupling beam $\Omega_c(\mathbf{r}) = \Omega_c\exp(ixq\theta_c)$ produces a uniform VP $\mathbf{A} = \hbar q\theta_c$, explaining the deflection effect via a momentary electric "kick" at the entrance of the cell $\mathbf{E}_{\rm in} = -\partial_t\mathbf{A} = \delta(t - t_{\rm in})\hbar q\theta_c\hat{\mathbf{x}}$, after which the probe propagates in a straight trajectory. A second kick at the existing face deflects the probe back to its original direction. Alternatively, a vortex coupling beam with a helical phase $\exp(im\phi)$ ($\phi$ the azimuthal angle) inflicts a kick in the azimuthal direction. The underlying VP $\mathbf{A} = \hbar m\nabla_\perp\phi$ implies an artificial magnetic field $B = \partial_x A_y - \partial_y A_x = 2\pi\delta(x)\delta(y)\hbar m$ along the dark vortex core, whereas the probe can propagate only at the brightened areas around the core. For example, a probe in the form of a ring of lobes is predicted to rotate while propagating in the medium (Yankelev, 2012).

## IV. COHERENT DIFFUSION OF STORED LIGHT

Diffusion and diffraction of dark-state polaritons, discussed in Sec. III, arise from the interplay between the atomic motion and the propagating excitation. Perhaps more elementary is the effect of the atomic motion on the atomic coherence in the absence of the light, as occurs during light storage. In light storage, the polariton is transformed into a matter-only excitation which does not propagate. The ground-state atomic coherence stores the light amplitude in the form of a spatial spin wave, later to be mapped back to a propagating polariton. Storage of light is accomplished with EIT by switching off the coupling beam—and switching it back on for retrieval (Liu *et al.*, 2001; Phillips *et al.*, 2001); see Fig. 13 (left). Storage and retrieval can also be performed with a longitudinal gradient of the frequency detunings. This method, known as gradient-echo memory (GEM), was recently implemented with ground-state coherence in a $\Lambda$ system (Hétet *et al.*, 2008).

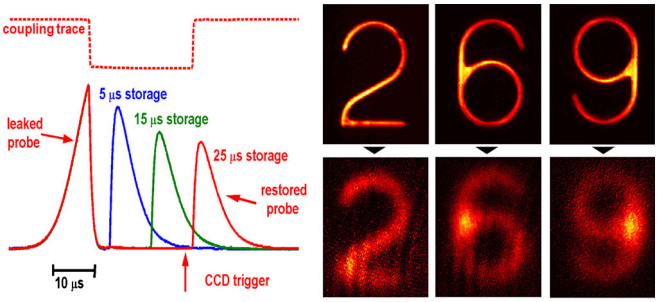


FIG. 13 (color online). Diffusion during storage of light in vapor. Left: The first half of the probe pulse is allowed to leak before storage. The second half is stored by turning off the coupling beam for a duration $\tau$ after which the probe revives. The traces show the probe for $\tau = 5$, 15, and 25 $\mu$s, and the coupling for $\tau = 25$ $\mu$s. Right: The spatial effect of diffusion is observed by comparing the images of the input probe (top row) and the retrieved probe (bottom row). Storage durations are $\tau = 2$, 6, and 9 $\mu$s. Adapted from Shuker *et al.*, 2008.

When light storage is performed with a single quantum, ideally by storing a single photon, it realizes a quantum memory—a fundamental building block for quantum communication and computation (Duan *et al.*, 2001; Hammerer, Sørensen, and Polzik, 2010). In atomic ensembles, the single quantum is stored in the collective state of all atoms. Unconditional storage of light on the level of single photons was recently achieved by Hosseini, Campbell *et al.* (2011) using GEM in a hot buffered cell. However, most of the experiments so far have used spontaneous Raman scattering to generate the spin wave, conditioned on the detection of a scattered photon (Chou *et al.*, 2004; Eisaman *et al.*, 2005; Matsukevich *et al.*, 2006; R. Zhao *et al.*, 2008; Bashkansky, Fatemi, and Vurgaftman, 2012). Diffusion of the atoms before the spin wave is converted back to light poses the same issues as in unconditional storage as described in this section.

### A. Diffusion of a stored coherence field

When storage is performed, the three-dimensional spatial envelope of the probe $\Omega(\mathbf{r})$ is linearly mapped onto the ground-state coherence[4] $\rho_{12}(\mathbf{r}, \tau = 0)$. The dynamics during the storage time $\tau$ is governed by

$$\partial_\tau \rho_{12}(\mathbf{r}, \tau) = D(\boldsymbol{\nabla} + i\mathbf{k})^2 \rho_{12}(\mathbf{r}, \tau) - \gamma_0 \rho_{12}(\mathbf{r}, \tau), \quad (18)$$

derived from Eq. (9) in the absence of light. Even for a uniform envelope and negligible damping ($\nabla \to 0$, $\gamma_0 \to 0$), the diffusion of atoms through the Raman wave results in a dephasing of rate $Dk^2$. Fleischhauer and Lukin (2002) and Mewes and Fleischhauer (2005) showed that the decoherence of the quantum memory (in terms of the storage fidelity) is proportional to this dephasing.

In a recent experiment, B. Zhao *et al.* (2008) showed that the memory time in a cold atomic gas reduces with the angle between the Raman beams and is determined by the time it takes the atoms to (ballistically) move one Raman wavelength ($\tau_d \propto k^{-1} \propto \theta^{-1}$). Indeed, memory times as long as milliseconds were achieved by B. Zhao *et al.* (2008) and by Zhang, Garner, and Hau (2009) using collinear beams ($k \approx 0$), and by R. Zhao *et al.* (2008) with an optical trap that confines the atomic motion in the direction of $\mathbf{k}$. Furthermore, Schnorrberger *et al.* (2009) demonstrated light storage with ultracold atoms trapped in a three-dimensional optical lattice (a Mott insulator). The confinement of atomic motion to a site much smaller than the optical wavelength allowed Schnorrberger *et al.* to imprint phase gradients of wave numbers $k = \theta q$, with $\theta$ as large as 25 mrad, while maintaining the memory for more than 0.1 ms. All this of course does not apply to a Bose-Einstein condensate (BEC) where, due to its long-range coherence, stored light was retrieved even after the atoms moved numerous $\lambda_R$ (Ginsberg, Garner, and Hau, 2007).

Nevertheless, even when $k \approx 0$, atomic motion plays an important role in the storage of finite-size and structured fields. Diffusion of the atomic coherence[5] $\partial_\tau \rho_{12} = D\nabla^2 \rho_{12}$ can be directly observed by comparing the input image to the retrieved image at different storage durations. This is especially true when the propagation time before and after storage is much shorter than the storage duration itself, as is often the case. Figure 13 (right) presents measurements of diffusion with stored images (Shuker *et al.*, 2008). Diffusion is clearly observed by the smearing of the digits' image and is more pronounced as the storage duration increases. The spreading of stored information was used by Zibrov *et al.* (2002) to perform storage and retrieval at two distant locations in the cell. As a complementary concept, Novikova, Xiao *et al.* (2005) demonstrated two retrievals from the same location due to diffusion of coherence out and back into the beam area.

We now take an ideal case with $k = 0$ and a coupling beam that covers the whole medium. Naively it might seem that the total power of the restored probe is not altered by diffusion as diffusion is a conserving process $\int \rho_{12} = \text{const}$. However, it is the light-field amplitude $\Omega \propto \rho_{12}$, rather than its intensity $|\Omega|^2$, that effectively diffuses, and the total power $P \propto \int |\Omega|^2$ decays. For example, a stored Gaussian beam that doubles its area due to diffusion conveys one-half of its initial power. This geometric effect was shown to limit the storage time of images and narrow beams in buffered cells (Shuker *et al.*, 2008; Hosseini, Sparkes *et al.*, 2011; Glorieux *et al.*, 2012).

In contrast to standard "heat" diffusion, stored images can be complex valued as the phase pattern of the probe is exactly imprinted on the diffusing coherence (Fleischhauer and Lukin, 2000). Patterned phase leads to effects of constructive and destructive interference during diffusion, similar to those occurring in light propagation. For instance, consider the diffusion of the annular ring shown in Fig. 14 (top). A flat-phased ring is completely filled up after a short storage time, while the dark center of a stored vortex ($LG_{01}$ mode) is well maintained. The vortex core remains dark due to destructive interference: the phase around the dark center completes a $2\pi$ twist, and the contributions of all atoms diffusing inward sum

[4]Alternatively, in spontaneous storage, the superposition of the coupling beam and a spontaneously generated photon heralding the storage is saved on the coherence field $\rho_{12}(\mathbf{r}, \tau = 0)$.

[5]Note that the ground-state populations $\rho_{11}(\mathbf{r})$ and $\rho_{22}(\mathbf{r})$ diffuse in a similar manner, but, in the weak-probe regime, their contribution to the storage is small.

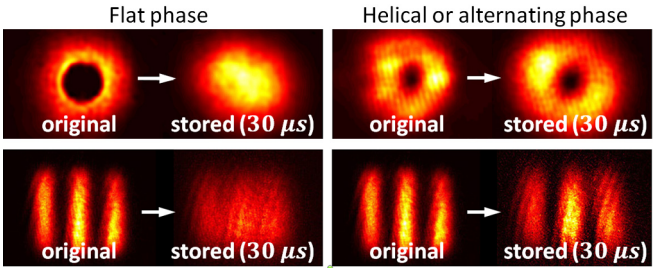


FIG. 14 (color online). Diffusion of coherence fields with uniform and nonuniform phase patterns. A flat-phased ring (top left) is filled up after a short storage duration, while a vortex ring with a helical phase is preserved (top right). Similarly, the blurring of a line pattern (bottom left) can be reduced by flipping the phase between adjacent lines (bottom right). As evident, the visibility of the lines with the alternating phase remains much higher than the flat-phased image. The vortex radius is 670 $\mu$m, the lines are 1.5/mm, and $D = 10$ cm$^2$/s. Adapted from Pugatch *et al.*, 2007, and Shuker *et al.*, 2008.

up to zero. Similar behavior is achieved by applying a well-designed phase pattern on specific images. The blurring of three resolution lines in Fig. 14 (bottom) is reduced by flipping the phase between adjacent lines. The decay of the lines' visibility due to diffusion is dramatically slowed down. Similar principles are used in optical phase-shift lithography to overcome the diffraction limit of small adjacent features. The downside of using destructive interference is the faster decay of the retrieved power. The decay rate increases with the complexity of the phase pattern, thereby decreasing the fidelity of the retrieved states (Wang *et al.*, 2008).

Other ideas requiring no *a priori* knowledge of the image were also studied. L. Zhao *et al.* (2008) suggested and Vudyasetu, Camacho, and Howell (2008) realized the storage of the Fraunhofer diffraction pattern of the image (see Fig. 15). Instead of filtering the high spatial components of the original image (a convolution with a Gaussian), diffusion merely attenuates its outermost parts (Gaussian multiplication), thereby maintaining its fine details. Cho, Oh, and Kim (2012) implemented a correlation-imaging technique, namely, ghost imaging, in which the retrieved light is recorded by a bucket detector and hence nearly unaffected by

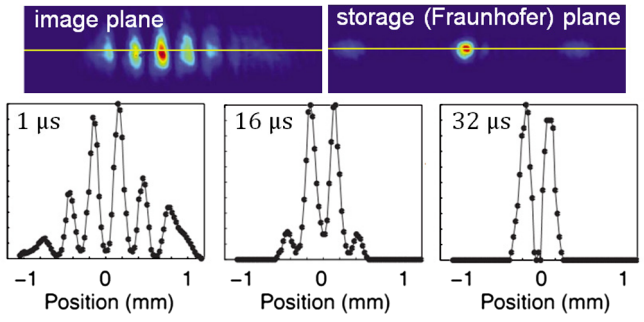


FIG. 15 (color online). By storing the Fraunhofer diffraction pattern (top right) instead of the image itself (top left) the fine details of the image are better preserved under diffusion (bottom). Rather, diffusion attenuates the outer parts of the beam. Adapted from Vudyasetu, Camacho, and Howell, 2008.

diffusion. This technique, however, required thousands of storage cycles to recover the image.

### B. Shape-preserving modes of coherent diffusion

In free-space optics, the paraxial-diffraction equation $\partial_z \Omega = i\nabla_\perp^2 \Omega/(2q)$ has several sets of shape-preserving solutions. These are notably the polynomial-Gaussian modes, including the well-known *standard* Hermite-Gauss (sHG) or Laguerre-Gauss (sLG) modes. Their transverse intensity pattern is maintained along the propagation direction $z$ and scaled according to the beam radius $w_z = w_0\sqrt{1 + (z/z_R)^2}$, where $z_R = qw_0^2/2$ is the Rayleigh distance. For example, the sHG mode $E_{n,m}^{\mathrm{sHG}}(x, y, z; w_0)$ has the form

$$H_n\left(\sqrt{2}\frac{x}{w_z}\right)H_m\left(\sqrt{2}\frac{y}{w_z}\right)\exp\left(-\frac{x^2+y^2}{\tilde{w}_z^2}\right),$$

where $\tilde{w}_z = \sqrt{2(z_R - iz)/q}$ is the complex radius and $H_k$ are the Hermite polynomials.

A less familiar solution for paraxial diffraction is the set of *elegant* modes, first studied by Siegman (1986) for their neater mathematical form. The elegant Hermite-Gauss (eHG) mode $E_{n,m}^{\mathrm{eHG}}(x, y, z; w_0)$ has the form

$$H_n\left(\frac{x}{\tilde{w}_z}\right)H_m\left(\frac{y}{\tilde{w}_z}\right)\exp\left(-\frac{x^2+y^2}{\tilde{w}_z^2}\right).$$

Contrast this with the standard mode above, here the polynomial and the Gaussian have a mutual (complex) scaling, and the $\sqrt{2}$ in the polynomial argument is absent. A corresponding elegant form for the circular-symmetric LG modes also exists.

The elegant modes are not shape preserving in free-space optics and are thus rarely used. Remarkably, at the focal plane ($z = 0$), they were found to be the basis for the shape-preserving solutions of coherent diffusion in two dimensions (Firstenberg *et al.*, 2010). Substituting $E_{n,m}^{\mathrm{eHG}} \Rightarrow \rho_{12}$ in Eq. (18) with $\mathbf{k} = 0$, one finds

$$E_{n,m}^{\mathrm{retrieved}}(\tau) = e^{-\gamma_0\tau}s(\tau)^{-(N+1)}E_{n,m}^{\mathrm{eHG}}(x, y, z = 0; w_\tau), \tag{19}$$

where $w_\tau = w_0 s(\tau)$ is the expanding waist radius, $s(\tau) = (1 + 4D\tau/w_0^2)^{1/2}$ is the stretching factor, and $N = n + m$ is the total mode order. The shape is therefore preserved, while expanding, throughout the diffusion. The algebraic decay $s(\tau)^{-2(N+1)}$ of the power $P \propto \int |E|^2$, explicated previously for the Gaussian ($N = 0$) case, becomes faster with increasing mode order due to interference between atoms diffusing through the oscillating phase patterns.

Note that the standard and elegant sets differ only in their polynomial terms, and therefore low-order HG and all vortices ($\mathrm{LG}_{p=0}$) are common to both sets and preserve their shape under the simultaneous action of diffusion and diffraction. They are thus the natural modes for slow light—a result which is standard and elegant, in both meanings of the words.

The diffusion of low-order (common) LG and HG modes during light storage in EIT is presented in Fig. 16. After scaling and normalization, the cross sections at different storage durations of each of the modes collapse to a single

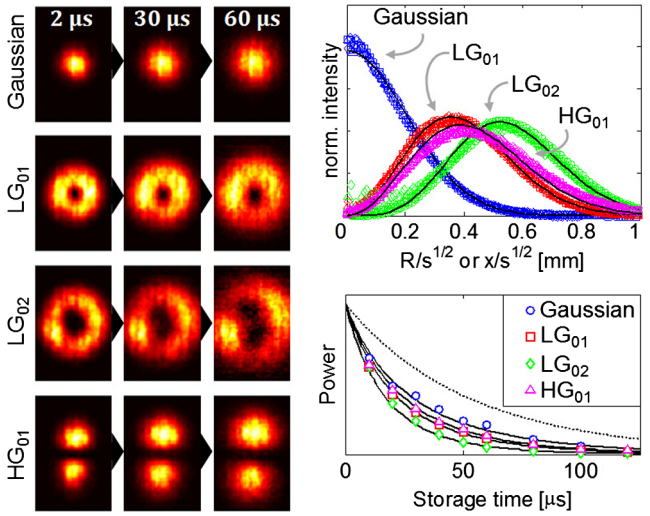


FIG. 16 (color online). Diffusion of "common" modes during storage. Left: Intensity patterns of (top to bottom) Gaussian, $LG_{01}$, $LG_{02}$, and $HG_{01}$, expanding due to diffusion while preserving their shape. Top right: Normalized cross sections at different storage durations, $\tau =$ (circles) 2, (squares) 20, (triangles) 40, and (diamonds) 60 $\mu$s, rescaled horizontally by the stretching factor $s(\tau)$. Bottom right: Decay of the total power, increasing with the total mode order $N$. The dashed line is $e^{-2\gamma\tau}$, and solid lines are $e^{-2\gamma\tau}s(\tau)^{-2(N+1)}$. Adapted from Firstenberg *et al.*, 2010.

curve. Higginbottom *et al.* (2012) used GEM to demonstrate the shape-preserving evolution of HG modes and the associated algebraic decay. By probing an optically pumped medium, the diffusion of LG beams with radial or azimuthal polarization (vector beams) was observed by Fatemi (2011). Yankelev *et al.* (2013) experimented with the high-order modes $sHG_{22}$ and $eHG_{22}$ (see Fig. 17). As expected, the shape of the $sHG_{22}$ mode is preserved during diffraction while dramatically altered during diffusion, and vice versa for the $eHG_{22}$.

Quite an interesting effect occurs when diffusion is performed away from the focal plane of the beam. The radial phase oscillations in the transverse plane, due to the curved phase fronts of the diverging beam, lead to destructive interference at the outskirts of the beam during diffusion. The result is a shape-preserving contraction of the beam, as shown in Fig. 18, in contrast to the obvious consequence of

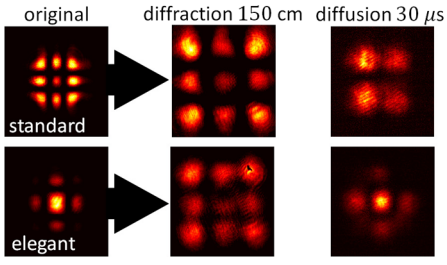


FIG. 17 (color online). Evolution of (top row) $sHG_{22}$ and (bottom row) $eHG_{22}$, measured by Yankelev *et al.* (2013), for (center column) diffraction in free space and (right column) diffusion during storage of light. The standard mode is preserved only during diffraction, whereas the elegant is preserved only during diffusion. Adapted from Yankelev *et al.*, 2013.

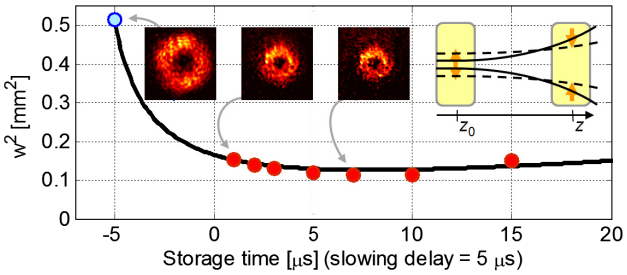


FIG. 18 (color online). Shape-preserving contraction and subsequent expansion of $LG_{01}$ during storage. Because of destructive interference, the diffusion of a diverging beam initially decreases the beam area $w_\tau^2$ (line is the theoretical prediction). Adapted from Firstenberg *et al.*, 2010.

diffusion. In effect, diffusion acts to (virtually) expand the waist radius at the focal plane ($z = 0$), even if this plane lies outside the medium, which leads initially to contraction at $|z| > z_R$ (see Fig. 18). This effect is directly related to the contraction of slow light out of focus, presented in Fig. 8.

## V. FINITE-SIZE BEAMS, RAMSEY NARROWING

Up until now, we mainly considered a large and uniform coupling beam, such that any inhomogeneity experienced by the atoms originated from the weak probe. In fact, the atoms are constantly driven toward the dark state by the perpetual coupling field, and those that are slow enough can adiabatically follow the local dark state $\propto \Omega_c^*|1\rangle - \Omega^*(\mathbf{r})|2\rangle$. However this situation is not prevalent, especially when the Raman fields (in a single or two beams) have a more symmetric role, such as in CPT and NMOR. There is often a finite "bright" region, covered by the light, and a remaining large "dark" region. The atomic motion within these regions and between them is the subject of this section.

Finite excitation times of ground-state coherence is a well-studied phenomena, as described by Gawlik (1986) and Arimondo (1996b), with the atoms either spatially leaving the illuminated area or shifting out of resonance due to some inhomogenous mechanism. The observed spectra are more elaborate than those we studied hitherto, because the finite pumping time rules out the linear response assumption. Instead of an instantaneous pumping action, the process becomes kinetic, with different atomic trajectories contributing differently to the spectra. An example of a non-Lorentzian, cusplike spectrum was presented by Pfleghaar *et al.* (1993). Pfleghaar *et al.* fully described the spectrum by using an exact geometrical transit-time model, taking into account the possible atomic trajectories through the inhomogenous beam. Trajectories with a transit time short compared to the pumping and damping rates $\tau_t \ll \gamma_0^{-1}, \gamma_P^{-1}$ contribute to the transit-time-limited broad feature; trajectories with long transit time contribute to the narrower central part of ultimate width $\gamma \approx \gamma_0 + \gamma_P$. We note here that non-Lorentzian spectra also arise for atoms at rest, when nonuniform power broadening dominates (Taichenachev *et al.*, 2004).

Coherently pumped atoms that have left the beam may return at a later time before losing their coherence. Coherent

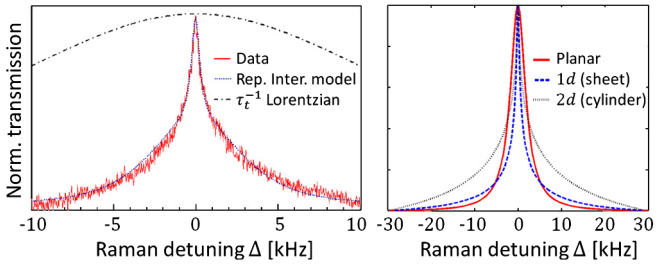


FIG. 19 (color online). Ramsey narrowing. Left: Dark-resonance spectrum for rubidium in 5 torr neon with 1-mm-wide beam, measured by Xiao *et al.* (2006) and calculated using the repeated-interactions model by Xiao, Novikova *et al.* (2008). The comparison to the transit-time ($\tau_t^{-1}$) broadening highlights the substantial Ramsey narrowing. Right: The diffusion solutions (21) by Firstenberg *et al.* (2008), for $2a = 0.2$ mm, $D = 10$ cm$^2$/s, no walls, and large power broadening $\gamma_p = 20\gamma_0 = 2$ kHz. Ramsey narrowing produces a central feature narrower than $2\gamma_p$. Adapted from Firstenberg *et al.*, 2008, and Xiao, Novikova *et al.*, 2008.

recurrence occurs in wall-coated or buffered cells and has long been known as a narrowing mechanism in standard rf spectroscopy (Robinson and Johnson, 1982). While the homogenous damping rate ($\gamma_0$) sets a lower limit on the width of any spectral feature, transit-time broadening ($\tau_t^{-1}$) is reduced by recurring atoms that effectively increase the interaction time, and power broadening ($\gamma_P$) is reduced because the recurring atoms have evolved predominantly in the dark. The initial pumping of the atoms in the bright region, the subsequent evolution in the dark, and their contribution to the spectrum upon return correspond to the Ramsey method of separated oscillating fields (Ramsey, 1950). The associated narrowing was therefore named *Ramsey narrowing*. For all-optical Raman resonances, Ramsey narrowing was first observed in wall-coated cells with NMOR (Kanorsky, Weis, and Skalla, 1995; Budker, Yashchuk, and Zolotorev, 1998), EIT (Klein *et al.*, 2006), and CPT (Breschi *et al.*, 2010). The measured spectra exhibit a broad pedestal feature, attributed to single-transit trajectories, and a narrow peak, due to coherent atoms recurring after long times in the dark (Budker *et al.*, 2002, 2005). Diffusion-induced Ramsey narrowing in a buffered cell was observed in various Raman processes (Zibrov, Novikova, and Matsko, 2001; Alipieva *et al.*, 2003; Novikova, Matsko, and Welch, 2005; Novikova, Xiao *et al.*, 2005), as exemplified in Fig. 19 (left).

The difficulty of writing a linear susceptibility in the form of Eq. (10) originates from the nonlinear terms in Eq. (9). Even for negligible power broadening $\gamma_P(\mathbf{r}) \to 0$, the source term $\Omega_c^*(\mathbf{r})\Omega(\mathbf{r})$ yields a convolution in $k$ space that, although accurate, makes it hard to solve for the spectrum. The following two approaches to calculate the spectrum thus stay in real space.

### A. Repeated interaction

Following the original ideas by Frueholz and Volk (1985), the repeated-interaction model builds the spectrum from an ensemble average of stochastic atomic trajectories, as delineated by Xiao, Novikova *et al.* (2008). Trajectories may comprise a single-transit time ($t_{\rm in}$), a Ramsey process ($t_{\rm in}/t_{\rm out}/t_{\rm in}$), or any longer sequence ($t_{\rm in}/t_{\rm out}/t_{\rm in}/t_{\rm out}/t_{\rm in}\cdots$). The contribution of longer trajectories is smaller due to the constant damping $\gamma_0$, and the sum thus converges. During the dark period, the ground-state dipole oscillates at the Raman-detuning frequency $\Delta$ with respect to the beating frequency of the Raman beams. An atom leaving the beams in a perfect dark state will have the probability $\mathrm{Re}[e^{-(i\Delta+\gamma_0)t_{\rm out}}]$ of returning in phase (in the dark state), resulting in Ramsey fringes with respect to $\Delta$. These can be measured by a fixed pulse sequence as shown in Fig. 20 (left). As with Ramsey spectroscopy, the fringes' period is set by the dark time $t_{\rm out}^{-1}$ and their envelope by the bright time $t_{\rm in}^{-1}$. Ramsey fringes were observed with Raman processes by separations in the velocity, time, and space domains (Buhr and Mlynek, 1986; Schuh *et al.*, 1993; Zibrov and Matsko, 2001; Zanon, Guerandel *et al.*, 2005).

Because of the distribution of the times spent in the bright and dark areas, a weighted average of such Ramsey fringes constitutes the spectrum. Xiao *et al.* (2006) calculated the time probability distribution of staying in the bright area $P_{\rm in}(t)$ and dark area $P_{\rm out}(t)$ for atoms diffusing through a cylindrical beam (see Fig. 20, right). A similar analysis for ballistic motion in wall-coated cells was carried out by Klein *et al.* (2011). The calculations assume two spatial dimensions, as the process is virtually insensitive to the axial motion of the atoms. If the dipole amplitude $d_0$ of an atom leaving the beam was fixed, the ensemble average would have read

$$\langle d\rangle = d_0\int_0^\infty dt P_{\rm out}(t)e^{-(i\Delta+\gamma_0)t} = d_0 P_{\rm out}(s), \tag{20}$$

where $s = i\Delta + \gamma_0$ and $P_{\rm out}(s)$ is the Laplace transform of $P_{\rm out}(t)$. The full repeated-interaction model involves nested integrals essentially similar to that of Eq. (20). To calculate the more intricate evolution in the bright stages, which involves dark-state pumping, Xiao, Novikova *et al.* (2008) followed Zanon, Tremine *et al.* (2005) and used the three-element vector model by Shahriar *et al.* (1997). The model reduces the master equation of the density matrix into a set of three Bloch equations, under the assumption of negligible $\gamma_0$. The evolution of the reduced vector has a closed mathematical solution in the form of a damped precession. A Ramsey sequence is then obtained by chaining three (in/out/in) solutions. Xiao, Novikova *et al.* (2008) generalized the vector

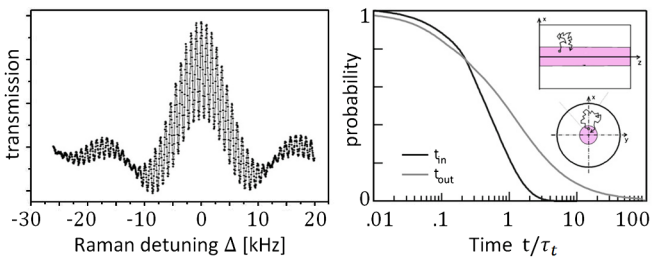


FIG. 20 (color online). Left: Ramsey fringes in a dark resonance, obtained by Zanon, Guerandel *et al.* (2005) with 80-$\mu$s pulses separated by 1 ms. Right: Probability distribution of the durations in the beam ($t_{\rm in}$) and in the dark ($t_{\rm out}$), calculated by Xiao *et al.* (2006) for atoms diffusing in a cylindrical geometry. Adapted from Zanon, Tremine *et al.*, 2005, and Xiao *et al.*, 2006.

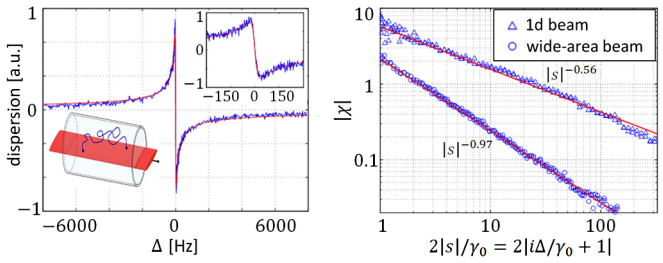


FIG. 21 (color online). Dispersion spectrum with a one-dimensional light sheet of width 126 $\mu$m. Right: Universal power laws with exponents $-1$ (Lorentzian) and $-0.5$ (one-dimensional recurrence). Adapted from Pugatch *et al.*, 2009.

model to account for finite $\gamma_0$ and obtained an analytic expression for all Ramsey spectra. Integrating over the trajectories using $P_{\rm in}(t)$ and $P_{\rm out}(t)$, the reconstructed spectrum agrees very well with the measurements (see Fig. 19, left) for a range of experimental parameters. Klein *et al.* (2011) augmented the model with a fourth atomic state, to account for optical pumping out of the $\Lambda$ system due to strong light fields. Indeed, for both ballistic and diffusing atoms, the distribution of bright times turns the Ramsey envelope into a broad spectral feature, while the distribution of dark times wipes out the Ramsey fringes, leaving a single pronounced narrow feature at the line center.

Recently, Pugatch *et al.* (2009) analyzed the limit of an infinitely small beam, for which the transit-time broadening, and hence the fringes envelope, is very large. Since $P_{\rm in}(t>0)\to 0$, the bright periods have a negligible effect on the spectrum, which becomes independent of the beam size and, in that respect, universal. While the atoms are essentially always in the dark, a nonzero ground-state dipole is sustained by the weak beam. The average dipole is given by an infinite sum of multiple periods in the dark, each one given by Eq. (20), $\langle d\rangle = d_0\sum_n P_{\rm out}(s)^n = d_0/[1-P_{\rm out}(s)]$. As evidenced by this expression, the resulting complex spectrum, measured by Pugatch *et al.* (2009) (see Fig. 21, left), constitutes a direct signature of the time distribution in the dark. Moreover, as the beam is infinitely small, $P_{\rm out}(t)$ is equivalent to the so-called first return-time distribution FRT($t$), which is the universal probability distribution for a random walker of returning to the origin at time $t$. In one-dimensional diffusion, corresponding to the sheetlike beam used in the experiment, $\mathrm{FRT}(s)=1-(4Ds)^{1/2}$, yielding $\langle d\rangle = d_0(4Ds)^{-1/2}$, in striking contrast to the complex Lorentzian spectrum $\langle d\rangle \propto s^{-1}$. These power-law decays are shown in Fig. 21, right.

### B. Diffusion solution

Although providing insight into the Ramsey-narrowing process, the repeated-interaction model applies the same physics already contained in the diffusion-equation formalism of the previous sections. One can essentially obtain the spectra from the coupled internal and external dynamics of the density-matrix distribution. To this end, we express the spatially dependent source and pumping rates, $S(\mathbf{r},t)$ and $\gamma_P(\mathbf{r})$ in Eq. (9), using the profiles of the beams $\Omega(x,y)$ and $\Omega_c(x,y)$ and then solve the diffusion equation for the steady-state distribution of the ground-state dipoles $\rho_{21}(x,y)$. The optical dipole $\rho_{31}(x,y)$ is calculated from Eq. (8), and an integration over the beam profile yields the absorption spectrum $P\propto \mathrm{Im}\int dxdy\Omega^*\rho_{31}$. As a matter of fact, such a mathematical procedure conflicts with the previous notion that steady-state solutions cannot accurately describe transit-time-limited spectra (Gawlik, 1986).

Xiao, Novikova *et al.* (2008) wrote a similar diffusion equation using the three-element vector model and by that generalized Eq. (9) to include a nonweak probe, and essentially any ratio between the Raman beams, including the balanced case. Numerical solution of the diffusion equation in this model, for a small Gaussian beam, was shown by Xiao *et al.* to agree with the repeated-interaction model.

For a few simple geometries, it is possible to obtain closed-form expressions for the spectra, as corrections $R(\Delta)$ to the stationary spectrum $\chi_0\to\chi_0(1-R)$ (Firstenberg *et al.*, 2008). For a stepwise light sheet (1D) or a top-hat beam (2D) of widths $2a$, and absorbing boundary conditions at the walls at a distance $b$, the diffusion solution gives

$$R^{\rm 1D}(\Delta)=\frac{1}{\kappa a}\frac{\tanh(\kappa a)}{1+(\kappa/\kappa_0)\tanh(\kappa a)\tanh[\kappa_0(b-a)]},$$
$$R^{\rm 2D}(\Delta)=\frac{2}{\kappa a}\left[\frac{I_0(\kappa a)}{I_1(\kappa a)}+\frac{\kappa}{\kappa_0}\frac{K_0(\kappa_0 a)}{K_1(\kappa_0 a)}(1-\beta)\right]^{-1}, \tag{21}$$

where $\beta=K_0(\kappa_0 b)K_0^{-1}(\kappa_0 a)I_0^{-1}[\kappa_0(b-a)]$ is due to the walls. Here $\kappa$ and $\kappa_0$ are defined via $D\kappa^2=\gamma_0+\gamma_p-i\Delta$ (inside the beam) and $D\kappa_0^2=\gamma_0-i\Delta$ (outside), and $I_n$, $K_n$ are the modified Bessel functions. These expressions revert to the transit-time limit for a circumferential wall ($b=a$) that depolarizes all atoms before they recur. The solution with no walls ($b\to\infty$) is shown in Fig. 19 (right), where the reduction of power broadening is clearly visible on the central feature. One may also recover the asymptotic universal behavior shown in Fig. 21 by taking $a\to 0$. Finally, minor corrections for nonflat beams were solved by Romanenko and Yatsenko (2008).

## VI. OUTLOOK

We presented the physics of Raman processes with hot atoms, whose internal coherence is preserved despite their external motion. The unique combination of rapid atomic motion, large Raman wavelengths, long lifetimes, and large group delays was shown to have diverse, significant spectral and spatial consequences. The same physical principles hold for a rich variety of Raman schemes and matter systems that are either out of the scope of this Colloquium or yet to be explored.

The spectra we studied derived from the exponential or Gaussian dephasing rate, pertaining to regular thermal motion. In two-dimensional systems, power-law decay of the velocity correlation is manifested by Lévy-like Raman spectra, whereas more intriguing spectra are expected for nonequilibrium one-dimensional systems. These are realizable with cold atoms, for which it is also exciting to explore anomalous diffusion, ballistic motion, and billiard dynamics. Oscillatory motion in a confining trap adds a modulated

component to the velocity correlation function, which is also measurable as periodic revivals of spatial structures.

Various matter-wave phenomena can find their analog in polariton diffusion, as diffusion manifests the diffraction equation in imaginary time. Thus, a speckle field of "traps" that locally depolarizes the dark state relates to the Anderson problem in one or two dimensions and is measurable spectrally and spatially. Here one can extend the study to the subdiffractive, subdiffusive ($\nabla^4$) evolution (Staliunas and Herrero, 2006) by controlling the slow-light parameters. Identifying the transverse modes of either ordered or disordered configurations is an important, instructive stage for understanding these systems (Wang and Genack, 2011). Extensions to the nonlinear realm can be performed with diffusion and diffraction manipulation in Raman four-wave mixing schemes, which will further allow optical conjugation and gain (Marino *et al.*, 2009; Katzir, Firstenberg, and Ron, 2012). These promising avenues, which represent a subset of what is currently being explored in this exciting field, are not only of fundamental interest, but could also have a profound impact on future quantum-technology applications.

## ACKNOWLEDGMENTS

We thank R. Pugatch for years of inspiring collaboration and gratefully acknowledge discussions with P. London, Y. Sagi, and D. Yanekelv. O. F. acknowledges support from the Harvard Quantum Optics Center. N. D. acknowledges support by the ISF, DIP, and Minerva foundations.

## APPENDIX: WEAK AND STRONG COLLISIONS

### 1. Weak-collisions formalism

Here we derive the Raman spectrum in the weak-collisions limit for stationary uniform fields (plane waves), a weak probe, and no power broadening. Assuming the $\Lambda$ atom of Fig. 3 travels along the classical trajectory $\mathbf{r} = \mathbf{r}(t)$, either ballistic or diffusive, we plug the time-dependent Rabi frequencies

$$\tilde{\Omega}(t) = \Omega e^{i\mathbf{q}\cdot\mathbf{r}(t) - i\omega t}, \quad \tilde{\Omega}_c(t) = \Omega_c e^{i\mathbf{q}_c\cdot\mathbf{r}(t) - i\omega_c t} \tag{A1}$$

into the Hamiltonian (5), with $\omega = c|\mathbf{q}|$ and $\omega_c = c|\mathbf{q}_c|$. To account for relaxations, the individual atom is represented by a density matrix $\rho^i_{ss'}(t)$ ($s, s' = 1, 2, 3$) in a master equation formalism; see, for example, Cyr, Tetu, and Breton (1993) and Nikonov *et al.* (1994). For brevity, we use a single decay rate $\Gamma$ for the two optical dipoles ($3 \leftrightarrow 1, 2$). The ground-state relaxation rate is $\gamma_0$. For a given atomic density $n_0$, the absorption of the probe is calculated from the imaginary part of the linear susceptibility $\chi(-\omega, \omega) = g\langle\rho^i_{31}(t)/\tilde{\Omega}(t)\rangle$, where $g = |\mathbf{q}|n_0|\mu_{31}|^2/\hbar\epsilon_0$ and $\langle\,\rangle \equiv \lim_{\tau\to\infty}\int_0^\tau dt/\tau$.

We assume that the equilibrium state of the atom in the absence of the probe is $|1\rangle\langle 1|$ ($\rho^{\rm eq}_{11} = 1$), regardless of the velocity and the instantaneous coupling power, which conforms with the limit of no power broadening. The first-order correction to the equilibrium state in the nonsaturated and weak-probe conditions $\Omega \ll \Omega_c \ll \Gamma$ involves only the ground-state dipole $\rho^i_{21}(t)$ and the probe transition dipole $\rho^i_{31}(t)$ (Kofman, 1997):

$$\begin{aligned}\frac{d}{dt}\rho^i_{31} &= i\tilde{\Omega}_c(t)\rho^i_{21} + i\tilde{\Omega}(t)\rho^{\rm eq}_{11} - i(\omega - \Delta_p - i\Gamma)\rho^i_{31},\\ \frac{d}{dt}\rho^i_{21} &= i\tilde{\Omega}^*_c(t)\rho^i_{31} - i(\omega - \omega_c - \Delta - i\gamma_0)\rho^i_{21}.\end{aligned} \tag{A2}$$

To obtain $\rho^i_{31}(t)$, Eqs. (A2) can be integrated and solved formally, by iterations up to first order in $\rho^i_{31}$, a valid approximation in the absence of power broadening $|\Omega_c^2| \ll \Gamma\gamma_0$. In this regime, the susceptibility becomes a sum $\chi(-\omega, \omega) = \chi_{\rm I}(\omega) - |\Omega_c^2|\chi_{\rm II}(\omega)$ of the Raman resonance $|\Omega_c^2|\chi_{\rm II}$ within the optical resonance $\chi_{\rm I}$ (Firstenberg *et al.*, 2007):

$$\chi_{\rm I} = g\left\langle i\int_0^t dt_1 e^{(-i\Delta_p - \Gamma)(t-t_1)} e^{i\Phi_{\rm I}}\right\rangle, \tag{A3a}$$

$$\chi_{\rm II} = g\left\langle i\int_0^t dt_1\int_0^{t_1} dt_2\int_0^{t_2} dt_3 \frac{e^{(-i\Delta_p - \Gamma_1)(t-t_1+t_2-t_3)}}{e^{-(i\Delta-\gamma_0)(t_1-t_2)}} e^{i\Phi_{\rm II}}\right\rangle. \tag{A3b}$$

The phases accumulated due to atomic motion though the light fields are $\Phi_{\rm I} = \mathbf{q}\cdot[\mathbf{r}(t) - \mathbf{r}(t_1)]$ and $\Phi_{\rm II} = \mathbf{q}_c\cdot[\mathbf{r}(t_1) - \mathbf{r}(t_2)] - \mathbf{q}\cdot[\mathbf{r}(t) - \mathbf{r}(t_3)]$. One may recognize a homogenous Lorentzian line $\int d\tau e^{(-i\Delta_p - \Gamma)\tau}$ in Eq. (A3a), broadened by the motional phase $\mathbf{q}\cdot\mathbf{r}(\tau)$.

We now invoke the weak-collisions limit, as laid out by Galatry (1961), Kubo (1962), and Rautian and Sobel'man (1967). Assuming a Gaussian process for the random variable $\Phi_{\rm I}$, together with a Markovian velocity relaxation $\langle\dot{\mathbf{r}}(t)\dot{\mathbf{r}}(t-\tau)\rangle = 3v_T^2 e^{-\gamma_c|\tau|}$, renders the dephasing $\langle e^{i\Phi_{\rm I}(t,t-\tau)}\rangle \approx e^{-\langle\Phi_{\rm I}^2\rangle/2} \approx e^{-|\mathbf{q}|^2\Lambda^2 H(\gamma_c\tau)}$, with $H(x) = e^{-x} - 1 + x$ and $\Lambda = v_T/\gamma_c$. The result is an optical spectrum in the form of a Gumbel distribution

$$\chi_{\rm I}(\Delta_p) = ig\int_0^\infty d\tau e^{(-i\Delta_p - \Gamma)\tau} e^{-|\mathbf{q}|^2\Lambda^2 H(\gamma_c\tau)}. \tag{A4}$$

The absorption line $\mathrm{Im}\chi_{\rm I}$ is shown in Fig. 5: At the Doppler limit $H(x) \approx x^2/2$ (solid black), it is a Gaussian $\exp(-\Delta_p^2/\Gamma^2_{\rm Doppler}/2)$; at the Dicke limit $H(x) \approx x$ (light gray), it is a Lorentzian $[\Gamma + \Gamma_{\rm Dicke}]/[\Delta^2 + (\Gamma + \Gamma_{\rm Dicke})^2]$; and in between (dark gray), it is neither.

A more elaborate but analogous derivation was performed by Firstenberg *et al.* (2007) for the Raman dephasing $\langle e^{i\Phi_{\rm II}}\rangle$, resulting in a closed integral form for $\chi_{\rm II}$. The Doppler-Dicke transition of the Raman resonance was thereby formally obtained for the first time, for the predominant case of a Doppler-broadened optical line and a nearly resonant coupling light:

$$\chi_{\rm II}(\Delta) = \frac{ig}{\Gamma^2}\int_0^\infty d\tau e^{(i\Delta - \gamma_0)\tau} e^{-k^2\Lambda^2 H(\gamma_c\tau)}. \tag{A5}$$

Remarkably, the transmission line (A5) has the same form as the absorption line (A4), with the Raman parameters ($k$, $\gamma_0$) replacing the optical parameters ($|\mathbf{q}|$, $\Gamma$).

### 2. Strong-collisions formalism

For the strong-collisions formalism, we use a density-matrix distribution function in space and velocity $\tilde{\varrho}_{ss'} = \tilde{\varrho}_{ss'}(\mathbf{r}, \mathbf{v}, t)$, constructed from the sum over (identical) individual atoms:

$$\tilde{\varrho}_{ss'} = \sum_i \rho^i_{ss'}(t)\delta(\mathbf{r}-\mathbf{r}_i(t))\delta(\mathbf{v}-\mathbf{v}_i(t)). \tag{A6}$$

This approach is general in that it allows atoms in different states to travel or diffuse between the illuminated and the dark areas, both in real spatial space and in velocity space, and thereby circumvents the approximation of an open system (Nikonov *et al.*, 1994). In a hot vapor, the density-matrix distribution can be taken as classical in the external-motion degrees of freedom, and evolves according to

$$(\partial_t + \mathbf{v}\cdot\boldsymbol{\nabla})\tilde{\varrho}_{ss'} + (\partial_t\tilde{\varrho}_{ss'})_{\mathrm{col}} = \sum_i (\partial_t\rho^i_{ss'})\delta(\mathbf{r}-\mathbf{r}_i(t))\delta(\mathbf{v}-\mathbf{v}_i(t)), \tag{A7}$$

where $(\partial_t\tilde{\varrho}_{ss'})_{\mathrm{col}}$ accounts for collisions. The right-hand side of Eq. (A7) describes the internal atomic dynamics, which can be taken from Eqs. (A2). Here, however, to set the stage for the description of polariton dynamics, we generalize Eqs. (A2) and employ a structured (time-dependent) probe and a structured (stationary) coupling:

$$\tilde{\Omega} = \Omega(\mathbf{r},t)e^{i\mathbf{q}\cdot\mathbf{r}-i\omega t}, \qquad \tilde{\Omega}_c = \Omega_c(\mathbf{r})e^{i\mathbf{q}_c\cdot\mathbf{r}-i\omega_c t}, \tag{A8}$$

where $\Omega(\mathbf{r},t)$ and $\Omega_c(\mathbf{r})$ are slowly varying envelopes of the Rabi frequencies. Correspondingly, we define the slowly varying atomic densities $\varrho_{31} = \tilde{\varrho}_{31}e^{i\omega t - i\mathbf{q}\cdot\mathbf{r}}$ and $\varrho_{21} = \tilde{\varrho}_{21}e^{i(\omega-\omega_c)t - i(\mathbf{q}-\mathbf{q}_c)\cdot\mathbf{r}}$.

We now assume that a single collision is strong enough to completely randomize the atomic velocity, so that the post-collision velocity is drawn from the equilibrium distribution $F(\mathbf{v})$ regardless of the precollision velocity. This assumption pertains to a Kubo-Anderson process, which in principle could be implemented in the individual-atom formalism used above for the weak-collisions limit (Brissaud and Frisch, 1974; Sagi *et al.*, 2010). In practice, however, calculating the four-time dephasing of the Raman resonance [$\Phi_{\mathrm{II}}$ in Eq. (A3b)] under the Kubo-Anderson assumptions is prohibitive. One thus resorts to a more direct approach and invokes a Boltzmann collision term with a single relaxation rate $\gamma_c$ (Nelkin and Ghatak, 1964):

$$(\partial_t\tilde{\varrho}_{ss'})_{\mathrm{col}} = -\gamma_c[\varrho_{ss'}(\mathbf{r},\mathbf{v},t) - \rho_{ss'}(\mathbf{r},t)F(\mathbf{v})], \tag{A9}$$

where the spatial density matrix is

$$\rho_{ss'}(\mathbf{r},t) = \int d^3v\,\varrho_{ss'}(\mathbf{r},\mathbf{v},t). \tag{A10}$$

The physical meaning of $\rho_{ss'}(\mathbf{r},t)$ is readily understood by identifying its diagonal elements $\rho_{ss}(\mathbf{r},t)$ as the spatial density of atoms at state $|s\rangle$, and its off-diagonal elements as the polarization density $\mathbf{P}(\mathbf{r},t)$, e.g., $\rho_{31}(\mathbf{r},t) = \boldsymbol{\varepsilon}\mathbf{P}_{31}(\mathbf{r},t)/\mu^*_{31}$. Note that Eq. (A9) does not consider pressure broadening, which we later introduced via the atomic decay rates (Corey and McCourt, 1984).

Finally, identifying $\rho^{\mathrm{eq}}_{11} \Rightarrow n_0F(\mathbf{v})$ in Eq. (A2) and substituting the definitions (A8)–(A10) into Eq. (A7), we obtain the equations of motion for the densities:

$$[\partial_t + \mathbf{v}\cdot\boldsymbol{\nabla} - i\delta_p(\mathbf{v})]\varrho_{31}(\mathbf{r},\mathbf{v},t) - i\Omega_c(\mathbf{r})\varrho_{21}(\mathbf{r},\mathbf{v},t) = \gamma_c\rho_{31}(\mathbf{r},t)F(\mathbf{v}) + i\Omega(\mathbf{r},t)n_0F(\mathbf{v}), \tag{A11a}$$

$$[\partial_t + \mathbf{v}\cdot\boldsymbol{\nabla} - i\delta(\mathbf{v})]\varrho_{21}(\mathbf{r},\mathbf{v},t) - i\Omega^*_c(\mathbf{r})\varrho_{31}(\mathbf{r},\mathbf{v},t) = \gamma_c\rho_{21}(\mathbf{r},t)F(\mathbf{v}), \tag{A11b}$$

where $\delta_p(\mathbf{v}) = \Delta_p - \mathbf{q}\cdot\mathbf{v} + i(\Gamma+\gamma_c)$ and $\delta(\mathbf{v}) = \Delta - (\mathbf{q}-\mathbf{q}_c)\cdot\mathbf{v} + i(\gamma_0+\gamma_c)$ are the Doppler-shifted complex detunings. These equations, together with a wave equation for the probe field, form the basis for the diffusion of polaritons presented in Secs. III and IV. To derive the Doppler-Dicke profiles at this stage, we restrict Eq. (A11) to stationary plane waves,

$$i\delta_1(\mathbf{v})\varrho_{31}(\mathbf{v}) + i\Omega_c\varrho_{21}(\mathbf{v}) = -(\gamma_c\rho_{31} + i\Omega n_0)F(\mathbf{v}), \tag{A12a}$$

$$i\delta(\mathbf{v})\varrho_{21}(\mathbf{v}) + i\Omega^*_c\varrho_{31}(\mathbf{v}) = -\gamma_c\rho_{21}F(\mathbf{v}). \tag{A12b}$$

From Eqs. (A12), Firstenberg *et al.* (2008) derived an exact integral form for the susceptibility $\chi = (g/n_0)\rho_{31}/\Omega$ and numerically exemplified the Doppler-Dicke transition of the dark resonance. The transition is similar to but not exactly as that found in the weak-collisions limit. For the sake of elucidation, we may examine the one-photon spectrum by substituting $\Omega_c = 0$,

$$\chi_1 = g\frac{G_1(\Delta_p)}{i\gamma_c G_1(\Delta_p) - 1}, \tag{A13}$$

where $G_1(\Delta_p)$ is the widely used Voigt profile:

$$G_1(\Delta_p) = \frac{1}{\sqrt{2\pi}v_T}\int du\frac{e^{-u^2/(2v_T^2)}}{\Delta_p - |\mathbf{q}|u + i(\Gamma+\gamma_c)}. \tag{A14}$$

The spectrum in the form of Eq. (A13) exhibits the Doppler-Dicke transition; see May (1999) and references therein. A comparison in Fig. 5 to the weak-collisions spectra reveals a maximal deviation of 10%–20% at the Doppler-Dicke crossover.

## REFERENCES


Akulshin, A. M., A. A. Celikov, and V. L. Velichansky, 1991, Opt. Commun. **84**, 139.

Alipieva, E., S. Gateva, E. Taskova, and S. Cartaleva, 2003, Opt. Lett. **28**, 1817.

Alzetta, G., A. Gozzini, L. Moi, and G. Orriols, 1976, Nuovo Cimento Soc. Ital. Fis. **36B**, 5.

Aminoff, C. G., and M. Pinard, 1982, J. Phys. France **43**, 263.

Andre, A., M. Bajcsy, A. S. Zibrov, and M. D. Lukin, 2005, Phys. Rev. Lett. **94**, 063902.

Arimondo, E., 1996a, Prog. Opt. **35**, 257.

Arimondo, E., 1996b, Phys. Rev. A **54**, 2216.

Arimondo, E., and G. Orriols, 1976, Lett. Nuovo Cimento Soc. Ital. Fis. **17**, 333.

Balabas, M. V., T. Karaulanov, M. P. Ledbetter, and D. Budker, 2010, Phys. Rev. Lett. **105**, 070801.

Bashkansky, M., F. K. Fatemi, and I. Vurgaftman, 2012, Opt. Lett. **37**, 142.

Berman, P. R., 1982, *New Trends in Atomic Physics*, Proceedings of the Les Houches Summer School, Session 38 (World Scientific, Singapore), Vol. 1, p. 451.

Berman, P. R., 2008, Contemp. Phys. **49**, 313.

Bicchi, P., L. Moi, P. Savino, and B. Zambon, 1980, Nuovo Cimento B **55B**, 1.

Bjorkholm, J. E., P. F. Liao, and A. Wokaun, 1982, Phys. Rev. A **26**, 2643.

Bloembergen, N., E. M. Purcell, and R. V. Pound, 1948, Phys. Rev. **73**, 679.

Bolkart, C., D. Rostohar, and M. Weitz, 2005, Phys. Rev. A **71**, 043816.

Boller, K.-J., A. Imamolu, and S. E. Harris, 1991, Phys. Rev. Lett. **66**, 2593.

Bortman-Arbiv, D., A. D. Wilson-Gordon, and H. Friedmann, 1998, Phys. Rev. A **58**, R3403.

Brandt, S., A. Nagel, R. Wynands, and D. Meschede, 1997, Phys. Rev. A **56**, R1063.

Breschi, E., G. Kazakov, C. Schori, G. Di Domenico, G. Mileti, A. Litvinov, and B. Matisov, 2010, Phys. Rev. A **82**, 063810.

Brissaud, A., and U. Frisch, 1974, J. Math. Phys. (N.Y.) **15**, 524.

Budker, D., W. Gawlik, D. F. Kimball, S. M. Rochester, V. V. Yashchuk, and A. Weis, 2002, Rev. Mod. Phys. **74**, 1153.

Budker, D., L. Hollberg, D. F. Kimball, J. Kitching, S. Pustelny, and V. V. Yashchuk, 2005, Phys. Rev. A **71**, 012903.

Budker, D., D. F. Kimball, S. M. Rochester, and V. V. Yashchuk, 1999, Phys. Rev. Lett. **83**, 1767.

Budker, D., and M. Romalis, 2007, Nat. Phys. **3**, 227.

Budker, D., V. Yashchuk, and M. Zolotorev, 1998, Phys. Rev. Lett. **81**, 5788.

Buhr, E., and J. Mlynek, 1986, Phys. Rev. Lett. **57**, 1300.

Camacho, R. M., C. J. Broadbent, I. Ali-Khan, and J. C. Howell, 2007, Phys. Rev. Lett. **98**, 043902.

Carvalho, P. R. S., L. E. E. de Araujo, and J. W. R. Tabosa, 2004, Phys. Rev. A **70**, 063818.

Cheng, J., and S. Han, 2007, Opt. Lett. **32**, 1162.

Cheng, J., S. Han, and Y. Yan, 2005, Phys. Rev. A **72**, 021801(R).

Cho, Y.-W., J.-E. Oh, and Y.-H. Kim, 2012, Phys. Rev. A **86**, 013844.

Chou, C. W., S. V. Polyakov, A. Kuzmich, and H. J. Kimble, 2004, Phys. Rev. Lett. **92**, 213601.

Ciuryło, R., R. Jaworski, J. Jurkowski, A. S. Pine, and J. Szudy, 2001, Phys. Rev. A **63**, 032507.

Corey, G. C., and F. R. McCourt, 1984, J. Chem. Phys. **81**, 2318.

Cyr, N., M. Tetu, and M. Breton, 1993, IEEE Trans. Instrum. Meas. **42**, 640.

Dalibard, J., F. Gerbier, G. Juzeliūnas, and P. Öhberg, 2011, Rev. Mod. Phys. **83**, 1523.

Dicke, R. H., 1953, Phys. Rev. **89**, 472.

Duan, L. M., M. D. Lukin, J. I. Cirac, and P. Zoller, 2001, Nature (London) **414**, 413.

Dutier, G., A. Yarovitski, S. Saltiel, A. Papoyan, D. Sarkisyan, D. Bloch, and M. Ducloy, 2003, Europhys. Lett. **63**, 35.

Eisaman, M. D., A. Andre, F. Massou, M. Fleischhauer, A. S. Zibrov, and M. D. Lukin, 2005, Nature (London) **438**, 837.

Erhard, M., and H. Helm, 2001, Phys. Rev. A **63**, 043813.

Erhard, M., S. Nußmann, and H. Helm, 2000, Phys. Rev. A **62**, 061802.

Ezekiel, S., S. Smith, M. Shahriar, and P. Hemmer, 1995, J. Lightwave Technol. **13**, 1189.

Fatemi, F. K., 2011, Opt. Express **19**, 25 143.

Feld, M. S., and A. Javan, 1969, Phys. Rev. **177**, 540.

Figueroa, E., F. Vewinger, J. Appel, and A. I. Lvovsky, 2006, Opt. Lett. **31**, 2625.

Firstenberg, O., P. London, M. Shuker, A. Ron, and N. Davidson, 2009, Nat. Phys. **5**, 665.

Firstenberg, O., P. London, D. Yankelev, R. Pugatch, M. Shuker, and N. Davidson, 2010, Phys. Rev. Lett. **105**, 183602.

Firstenberg, O., M. Shuker, A. Ben-Kish, D. R. Fredkin, N. Davidson, and A. Ron, 2007, Phys. Rev. A **76**, 013818.

Firstenberg, O., M. Shuker, N. Davidson, and A. Ron, 2009, Phys. Rev. Lett. **102**, 043601.

Firstenberg, O., M. Shuker, R. Pugatch, D. R. Fredkin, N. Davidson, and A. Ron, 2008, Phys. Rev. A **77**, 043830.

Fleischhauer, M., A. Imamoglu, and J. P. Marangos, 2005, Rev. Mod. Phys. **77**, 633.

Fleischhauer, M., and M. D. Lukin, 2000, Phys. Rev. Lett. **84**, 5094.

Fleischhauer, M., and M. D. Lukin, 2002, Phys. Rev. A **65**, 022314.

Friedler, I., G. Kurizki, O. Cohen, and M. Segev, 2005, Opt. Lett. **30**, 3374.

Frueholz, R. P., and C. H. Volk, 1985, J. Phys. B **18**, 4055.

Galatry, L., 1961, Phys. Rev. **122**, 1218.

Gawlik, W., 1986, Phys. Rev. A **34**, 3760.

Ghosh, J., R. Ghosh, F. Goldfarb, J.-L. Le Gouët, and F. Bretenaker, 2009, Phys. Rev. A **80**, 023817.

Gibble, K. E., and A. Gallagher, 1991, Phys. Rev. A **43**, 1366.

Ginsberg, N. S., S. R. Garner, and L. V. Hau, 2007, Nature (London) **445**, 623.

Glorieux, Q., J. B. Clark, A. M. Marino, Z. Zhou, and P. D. Lett, 2012, Opt. Express **20**, 12 350.

Goldfarb, F., J. Ghosh, M. David, J. Ruggiero, T. Chaneliere, J.-L. L. Gouet, H. Gilles, R. Ghosh, and F. Bretenaker, 2008, Europhys. Lett. **82**, 54 002.

Graf, M., E. Arimondo, E. S. Fry, D. E. Nikonov, G. G. Padmabandu, M. O. Scully, and S.-Y. Zhu, 1995, Phys. Rev. A **51**, 4030.

Hammerer, K., A. S. Sørensen, and E. S. Polzik, 2010, Rev. Mod. Phys. **82**, 1041.

Hänsch, T. W., I. S. Shahin, and A. L. Schawlow, 1971, Phys. Rev. Lett. **27**, 707.

Happer, W., 1972, Rev. Mod. Phys. **44**, 169.

Harris, S. E., 1997, Phys. Today **50**, No. 7, 36.

Harris, S. E., and L. V. Hau, 1999, Phys. Rev. Lett. **82**, 4611.

Hau, L., S. E. Harris, Z. Dutton, and C. H. Behroozi, 1999, Nature (London) **397**, 594.

Hétet, G., M. Hosseini, B. M. Sparkes, D. Oblak, P. K. Lam, and B. C. Buchler, 2008, Opt. Lett. **33**, 2323.

Higginbottom, D. B., B. M. Sparkes, M. Rancic, O. Pinel, M. Hosseini, P. K. Lam, and B. C. Buchler, 2012, Phys. Rev. A **86**, 023801.

Hong, T., 2003, Phys. Rev. Lett. **90**, 183901.

Hosseini, M., G. Campbell, B. M. Sparkes, P. K. Lam, and B. C. Buchler, 2011, Nat. Phys. **7**, 794.

Hosseini, M., B. M. Sparkes, G. Campbell, P. K. Lam, and B. Buchler, 2011, Nat. Commun. **2**, 174.

Hosseini, M., B. M. Sparkes, G. T. Campbell, P. K. Lam, and B. C. Buchler, 2012, J. Phys. B **45**, 124004.

Jain, M., A. J. Merriam, A. Kasapi, G. Y. Yin, and S. E. Harris, 1995, Phys. Rev. Lett. **75**, 4385.

Javan, A., O. Kocharovskaya, H. Lee, and M. O. Scully, 2002, Phys. Rev. A **66**, 013805.

Kanorsky, S. I., A. Weis, and J. Skalla, 1995, Appl. Phys. B **60**, S165.

Kapoor, R., and G. S. Agarwal, 2000, Phys. Rev. A **61**, 053818.

Kasapi, A., M. Jain, G. Y. Yin, and S. E. Harris, 1995, Phys. Rev. Lett. **74**, 2447.

Kash, M. M., V. A. Sautenkov, A. S. Zibrov, L. Hollberg, G. R. Welch, M. D. Lukin, Y. Rostovtsev, E. S. Fry, and M. O. Scully, 1999, Phys. Rev. Lett. **82**, 5229.
Katzir, I., O. Firstenberg, and A. Ron, 2012 (unpublished).
Keilson, J., and K. E. Storer, 1952, Q. Appl. Math. **10**, 243.
Klein, M., M. Hohensee, D. F. Phillips, and R. L. Walsworth, 2011, Phys. Rev. A **83**, 013826.
Klein, M., I. Novikova, D. F. Phillips, and R. L. Walsworth, 2006, J. Mod. Opt. **53**, 2583.
Knappe, S., V. Shah, P. D. D. Schwindt, L. Hollberg, J. Kitching, L.-A. Liew, and J. Moreland, 2004, Appl. Phys. Lett. **85**, 1460.
Kocharovskaya, O., Y. Rostovtsev, and M. O. Scully, 2001, Phys. Rev. Lett. **86**, 628.
Kofman, A. G., 1997, Phys. Rev. A **56**, 2280.
Kominis, I. K., T. W. Kornack, J. C. Allred, and M. V. Romalis, 2003, Nature (London) **422**, 596.
Kubo, R., 1962, *Fluctuation, Relaxation and Resonance in Magnetic Systems* (Plenum, New York).
Lee, H., Y. Rostovtsev, C. Bednar, and A. Javan, 2003, Appl. Phys. B **76**, 33.
Liu, C., Z. Dutton, C. H. Behroozi, and L. Hau, 2001, Nature (London) **409**, 490.
Lukin, M. D., 2003, Rev. Mod. Phys. **75**, 457.
Marino, A. M., R. C. Pooser, V. Boyer, and P. D. Lett, 2009, Nature (London) **457**, 859.
Matsukevich, D. N., T. Chanelière, S. D. Jenkins, S.-Y. Lan, T. A. B. Kennedy, and A. Kuzmich, 2006, Phys. Rev. Lett. **97**, 013601.
May, A. D., 1999, Phys. Rev. A **59**, 3495.
McGuyer, B. H., R. Marsland, B. A. Olsen, and W. Happer, 2012, Phys. Rev. Lett. **108**, 183202.
Mewes, C., and M. Fleischhauer, 2005, Phys. Rev. A **72**, 022327.
Mitsunaga, M., M. Yamashita, and H. Inoue, 2000, Phys. Rev. A **62**, 013817.
Morgan, S. W., and W. Happer, 2010, Phys. Rev. A **81**, 042703.
Moseley, R. R., S. Shepherd, D. J. Fulton, B. D. Sinclair, and M. H. Dunn, 1995, Phys. Rev. Lett. **74**, 670.
Nagel, A., C. Affolderbach, S. Knappe, and R. Wynands, 1999, Phys. Rev. A **61**, 012504.
Nelkin, M., and A. Ghatak, 1964, Phys. Rev. **135**, A4.
Nikonov, D. E., U. W. Rathe, M. O. Scully, S.-Y. Zhu, E. S. Fry, X. Li, G. G. Padmabandu, and M. Fleischhauer, 1994, Quantum Opt. **6**, 245.
Novikova, I., A. B. Matsko, and G. R. Welch, 2005, J. Opt. Soc. Am. B **22**, 44.
Novikova, I., Y. Xiao, D. F. Phillips, and R. L. Walsworth, 2005, J. Mod. Opt. **52**, 2381.
Ottinger, C., R. Scheps, G. W. York, and A. Gallagher, 1975, Phys. Rev. A **11**, 1815.
Peach, G., 1981, Adv. Phys. **30**, 367.
Pendry, J. B., 2000, Phys. Rev. Lett. **85**, 3966.
Peyronel, T., O. Firstenberg, Q.-Y. Liang, S. Hofferberth, A. V. Gorshkov, T. Pohl, M. D. Lukin, and V. Vuletic, 2012, Nature (London) **488**, 57.
Pfleghaar, E., J. Wurster, S. I. Kanorsky, and A. Weis, 1993, Opt. Commun. **99**, 303.
Phillips, D. F., A. Fleischhauer, A. Mair, R. L. Walsworth, and M. D. Lukin, 2001, Phys. Rev. Lett. **86**, 783.
Pugatch, R., O. Firstenberg, M. Shuker, and N. Davidson, 2009, Phys. Rev. Lett. **102**, 150602.
Pugatch, R., M. Shuker, O. Firstenberg, A. Ron, and N. Davidson, 2007, Phys. Rev. Lett. **98**, 203601.
Ramsey, N. F., 1950, Phys. Rev. **78**, 695.
Rautian, S. G., and I. I. Sobel'man, 1967, Sov. Phys. Usp. **9**, 701.
Robinson, H. G., and C. E. Johnson, 1982, Appl. Phys. Lett. **40**, 771.
Romanenko, A., and L. Yatsenko, 2008, arXiv:0801.3436.
Rothberg, L. J., and N. Bloembergen, 1984, Phys. Rev. A **30**, 820.
Sagi, Y., R. Pugatch, I. Almog, and N. Davidson, 2010, Phys. Rev. Lett. **104**, 253003.
Schnorrberger, U., J. D. Thompson, S. Trotzky, R. Pugatch, N. Davidson, S. Kuhr, and I. Bloch, 2009, Phys. Rev. Lett. **103**, 033003.
Schuh, B., S. Kanorsky, A. Weis, and T. Hnsch, 1993, Opt. Commun. **100**, 451.
Shahriar, M. S., P. R. Hemmer, D. P. Katz, A. Lee, and M. G. Prentiss, 1997, Phys. Rev. A **55**, 2272.
Shuker, M., O. Firstenberg, R. Pugatch, A. Ben-Kish, A. Ron, and N. Davidson, 2007, Phys. Rev. A **76**, 023813.
Shuker, M., O. Firstenberg, R. Pugatch, A. Ron, and N. Davidson, 2008, Phys. Rev. Lett. **100**, 223601.
Shwa, D., E. Shtranvasser, Y. Shalibo, and N. Katz, 2012, Opt. Express **20**, 24 835.
Siegman, A. E., 1986, *Lasers* (University Science Books, Sausalito, CA).
Smiciklas, M., J. M. Brown, L. W. Cheuk, S. J. Smullin, and M. V. Romalis, 2011, Phys. Rev. Lett. **107**, 171604.
Staliunas, K., and R. Herrero, 2006, Phys. Rev. E **73**, 016601.
Taichenachev, A. V., A. M. Tumaikin, V. I. Yudin, M. Stahler, R. Wynands, J. Kitching, and L. Hollberg, 2004, Phys. Rev. A **69**, 024501.
Tarhan, D., N. Postacioglu, and Özgür E. Müstecaplioglu, 2007, Opt. Lett. **32**, 1038.
Tilchin, E., A. D. Wilson-Gordon, and O. Firstenberg, 2011, Phys. Rev. A **83**, 053812.
Torrey, H. C., 1956, Phys. Rev. **104**, 563.
Truscott, A. G., M. E. J. Friese, N. R. Heckenberg, and H. Rubinsztein-Dunlop, 1999, Phys. Rev. Lett. **82**, 1438.
Vaselago, V. G., 1968, Sov. Phys. Usp. **10**, 509.
Vasilyev, D. V., I. V. Sokolov, and E. S. Polzik, 2010, Phys. Rev. A **81**, 020302.
Vengalattore, M., and M. Prentiss, 2005, Phys. Rev. Lett. **95**, 243601.
Vudyasetu, P. K., R. M. Camacho, and J. C. Howell, 2008, Phys. Rev. Lett. **100**, 123903.
Walker, T. G., 1989, Phys. Rev. A **40**, 4959.
Walker, T. G., and W. Happer, 1997, Rev. Mod. Phys. **69**, 629.
Wang, J., and A. Z. Genack, 2011, Nature (London) **471**, 345.
Wang, T., L. Zhao, L. Jiang, and S. F. Yelin, 2008, Phys. Rev. A **77**, 043815.
Xiao, Y., 2009, Mod. Phys. Lett. B **23**, 661.
Xiao, Y., M. Klein, M. Hohensee, L. Jiang, D. F. Phillips, M. D. Lukin, and R. L. Walsworth, 2008, Phys. Rev. Lett. **101**, 043601.
Xiao, Y., I. Novikova, D. F. Phillips, and R. L. Walsworth, 2006, Phys. Rev. Lett. **96**, 043601.
Xiao, Y., I. Novikova, D. F. Phillips, and R. L. Walsworth, 2008, Opt. Express **16**, 14 128.
Yankelev, D., 2012, Spatial Phenomena of Finite Beams in EIT Medium, Master's thesis, Technion-Israel Institute of Technology, Haifa, Israel.
Yankelev, D., O. Firstenberg, M. Shuker, and N. Davidson, 2013, Opt. Lett. **38**, 1203.
Ye, C. Y., and A. S. Zibrov, 2002, Phys. Rev. A **65**, 023806.
Zanon, T., S. Guerandel, E. de Clercq, D. Holleville, N. Dimarcq, and A. Clairon, 2005, Phys. Rev. Lett. **94**, 193002.
Zanon, T., S. Tremine, S. Guerandel, E. de Clercq, D. Holleville, N. Dimarcq, and A. Clairon, 2005, IEEE Trans. Instrum. Meas. **54**, 776.
Zhang, R., S. R. Garner, and L. V. Hau, 2009, Phys. Rev. Lett. **103**, 233602.

Zhao, B., Y.-A. Chen, X.-H. Bao, T. Strassel, C.-S. Chuu, X.-M. Jin, J. Schmiedmayer, Z.-S. Yuan, S. Chen, and J.-W. Pan, 2008, Nat. Phys. **5**, 95.

Zhao, L., T. Wang, Y. Xiao, and S. F. Yelin, 2008, Phys. Rev. A **77**, 041802.

Zhao, R., Y. O. Dudin, S. D. Jenkins, C. J. Campbell, D. N. Matsukevich, T. A. B. Kennedy, and A. Kuzmich, 2008, Nat. Phys. **5**, 100.

Zibrov, A. S., and A. B. Matsko, 2001, Phys. Rev. A **65**, 013814.

Zibrov, A. S., A. B. Matsko, O. Kocharovskaya, Y. V. Rostovtsev, G. R. Welch, and M. O. Scully, 2002, Phys. Rev. Lett. **88**, 103601.

Zibrov, A. S., I. Novikova, and A. B. Matsko, 2001, Opt. Lett. **26**, 1311.

See Supplemental Material at http://link.aps.org/supplemental/10.1103/RevModPhys.85.941 for an illustration of the Doppler-Dicke transition for a moving acoustic emitter.